





## Article

# Natural and Anthropogenic Groundwater Contamination in a Coastal Volcanic-Sedimentary Aquifer: The Case of the Archaeological Site of *Cumae* (Phlegraean Fields, Southern Italy)

Luisa Stellato <sup>1,\*</sup>, Silvio Coda <sup>2</sup>, Michele Arienzo <sup>2</sup>, Pantaleone De Vita <sup>2</sup>, Brunella Di Rienzo <sup>1</sup>, Antonio D'Onofrio <sup>1</sup>, Luciano Ferrara <sup>3</sup>, Fabio Marzaioli <sup>1</sup>, Marco Trifuoggi <sup>3</sup> and Vincenzo Allocca <sup>2,\*</sup>

<sup>1</sup> Centre for Isotopic Research on Cultural and Environmental Heritage (CIRCE), Dipartimento di Matematica e Fisica, Università degli Studi della Campania Luigi Vanvitelli, Viale Lincoln 5, 81100 Caserta, Italy; brunella.dirienzo@unicampania.it (B.D.R.); antonio.donofrio@unicampania.it (A.D.); fabio.marzaioli@unicampania.it (F.M.)

<sup>2</sup> Dipartimento di Scienze della Terra, dell'Ambiente e delle Risorse, Università degli Studi di Napoli Federico II, Complesso Universitario di Monte S. Angelo, via Cintia, 80126 Naples, Italy; silvio.coda@unina.it (S.C.); michele.arienzo@unina.it (M.A.); pantaleone.devita@unina.it (P.D.V.)

<sup>3</sup> Dipartimento di Scienze Chimiche, Università degli Studi di Napoli Federico II, Complesso Universitario di Monte S. Angelo, via Cintia, 80126 Naples, Italy; luciano.ferrara@unina.it (L.F.); marco.trifuoggi@unina.it (M.T.)

\* Correspondence: luisa.stellato@unicampania.it (L.S.); vincenzo.allocca@unina.it (V.A.); Tel.: +39-347-6037825 (L.S.); +39-380-5245873 (V.A.)

Received: 27 October 2020; Accepted: 6 December 2020; Published: 9 December 2020



**Abstract:** Archeological sites close to coastal volcanic-sedimentary aquifers are threatened by groundwater contaminated by natural and anthropogenic processes. The paper reports on a hydrogeological, chemical (major, minor and trace elements) and isotopic ( $\delta D-H_2O$ ,  $\delta^{18}O-H_2O$ ,  $\delta^{15}N-NO_3$ ,  $\delta^{18}O-NO_3$ ,  $\delta^{11}B$ ,  $^{222}Rn$ ) survey of groundwater at the *Cumae* archaeological site, which is located in the coastal north-western sector of the volcanic district of Phlegraean Fields (southern Italy), where groundwater flooding phenomena occur. Results show the presence of a complex coastal volcanic-sedimentary aquifer system where groundwater quality is influenced mainly by: (i) aquifer lithology and localized ascent of magmatic fluids along buried volcano-tectonic discontinuities, (ii) mixing of groundwater, deep mineralized fluids and seawater during groundwater pumping, and (iii) nitrate contamination  $>50$  mg/L from non-point agricultural sources. Moreover,  $\delta D$  and  $\delta^{18}O$  point toward fast recharge from seasonal precipitations, while the isotopic ratios of N and O in nitrate reveal the contribution of mineral and organic fertilizers as well as leakage from septic tanks. Results can assist the local archaeological authority for the safeguarding and management of the archaeological heritage of the *Cumae* site.

**Keywords:** coastal volcanic-sedimentary aquifer; natural and anthropogenic contamination;  $^{222}Rn$ ; water isotopes; nitrate isotopes; archaeological site; Phlegraean Fields; southern Italy

## 1. Introduction

Coastal aquifers are generally used to supply freshwater, especially in arid and semiarid areas [1]. More than 60% of the global population is concentrated in coastal areas comprising only 10% of the Earth's surface. This percentage is expected to rise to 75% [2,3]. Water use for anthropic activities is a key driver in the hydrologic regime of coastal aquifers [4] and demand for both human consumption

and agricultural/industrial uses [5] threatens water resources. This is even more dramatic in arid and semiarid areas where periods of higher demand for freshwater coincide with those of greater water scarcity [2]. According to the Intergovernmental Panel on Climate Change (IPCC) [6], the vulnerability of a coastal aquifer is the degree of being influenced or coping with sea-level rise and/or groundwater abstraction. Hence, coastal aquifer water quality can be endangered by high groundwater demand related to population growth and climate changes leading to a change of the dynamic equilibrium between fresh groundwater and seawater intrusion [4,7–9].

In coastal aquifers, salinization induced by seawater intrusion and human activities are the most important cause of groundwater degradation [10,11]. Therefore, an effective and targeted management is needed in order to preserve water resources in such complex systems [11–13]. Among anthropic activities, agricultural practices (use of mineral and/or organic fertilizers and groundwater abstraction) are the more frequent causes of groundwater quality deterioration [12]. In fact, fertilization and irrigation increase nutrient concentration in groundwater above threshold values, especially for dissolved nitrate, released mainly by the use of synthetic and natural fertilizers (91/676/CE EU Directive). Nitrate is especially dangerous for children and old people because it interacts with hemoglobin, hindering oxygen flow to cells (methemoglobinemia) [14], and can also form nitrosamine, which is considered to be a carcinogenic compound [15,16]. Septic tanks and sewage systems can also release total inorganic nitrogen to groundwater bodies [17,18]. Moreover, nitrogen compounds can also promote, together with phosphorous, eutrophication of freshwater bodies of rivers, lakes and marshy areas of coastal zones [19–21]. In sedimentary-volcanic aquifers proximal to an active volcanic system, as in the present study, the upwelling highly mineralized fluids can also cause groundwater mineralization and, as a consequence, have an impact on archaeological artifacts and infrastructure [22–24].

The major concern of local authorities in charge of managing water resources in such complex systems is the identification of the sources of pollution and the comprehension of processes influencing the concentration of contaminants in groundwater, aimed at planning effective countermeasures for groundwater bodies' quality protection and restoration [8]. However, the identification of pollution sources is not an easy task because of the presence of: (1) more than one source, (2) point and diffuse sources and (3) several biogeochemical processes which can alter contaminant concentration [25]. The management of water resources in a coastal area requires an accurate characterization of aquifers' recharge, groundwater pathways and identification of groundwater contamination sources which can be effectively carried out by an integrated hydrogeological, hydrostratigraphical, hydrochemical and isotopic assessment [26–29]. In many cases, the use of stable isotopes of elements allows the identification of sources characterized by different isotopic compositions [14,30–34]. In particular, the measurement of natural and anthropogenic isotopic tracers can provide information about groundwater recharge and mixing ( $\delta D$  and  $\delta^{18}O$ ) [35–38], help identify groundwater hydro-facies and seawater intrusion (major ions and trace elements) [27,39–41], can give information about the upwelling of mineralized fluids as well as aquifers' homogeneity ( $^{222}Rn$ ,  $\delta^{11}B$ ) [42–45] and identify nitrate pollution sources ( $\delta^{15}N$  and  $\delta^{18}O$  of nitrates,  $\delta^{11}B$ ) [25,34,46–48].

In recent years, archaeological research carried out in coastal plains of southern Italy [49–51] and archaeological sites of the Mediterranean region [52] has seen a setback including reburial of some artefacts, due to rising groundwater and consequent flooding, as observed in the *Cumae* archaeological site (in the province of Naples) which is among the most important and visited in southern Italy. It is located within the Phlegraean Fields Regional Park, which hosts a large supervolcano situated to the west of Naples [53] and in 2006 has been included in the World Heritage sites of UNESCO. The *Cumae* archaeological site hosts the partially buried ruins of the Greek to medieval city of *Cumae*. The site includes different artefacts, cultural remains and ancient monuments, dating back to the Greek, Roman and Byzantine epochs [54]. In particular, the Monumental Roman Necropolis, a small sub-flat coastal plain area, has been studied since 1809 and archaeological research still continues.

Given the relevance of this archaeological site, the conservation and protection of ancient ruins is a principal task. The deterioration of in situ archaeological deposits [55] can be accelerated by environmental and hydrogeological changes. Moreover, the conservation and management of archaeological resources, especially in rural areas, is threatened by the use of fertilizers and pesticides, irrigations, tillage and drainage. In particular, the lithology of the buried artifacts can be damaged by corroding compounds bearing groundwater [56,57].

Considering the interference between groundwater and archaeological structures, a multidisciplinary approach based on a hydrogeological, hydrogeochemical and isotopic monitoring has been adopted in order to characterize the natural and anthropogenic processes affecting groundwater quality in the *Cumae* coastal aquifer. The measurements concerned water levels, temperature, pH, electric conductivity, major and minor ion concentrations, trace elements and isotopes ( $\delta D-H_2O$ ,  $\delta^{18}O-H_2O$ ,  $\delta^{15}N-NO_3$ ,  $\delta^{18}O-NO_3$ ,  $\delta^{11}B$ ,  $^{222}Rn$ ). The analysis of the temporal and spatial distributions of each parameter and the identification of natural and anthropic sources of groundwater contamination are central to assessing the potential threat to these ancient ruins.

## 2. Description of the Study Area

The *Cumae* archaeological site extends over about 3.0 km<sup>2</sup> and is located in the north-western coastal sector of the active volcanic district of the Phlegraean Fields bordering the Tyrrhenian coast of southern Italy (Figure 1a,b). It is part of the Phlegraean wetlands area and of Mount Cumae's coastal Forest, both belonging to the Phlegraean Fields Regional Park. It includes the ancient city of *Kyme*, the first Greek colony in Italy founded in the 730 B.C. and inhabited until 1207 A.C. [53].

During the Holocene, primary and secondary volcanism of the Phlegraean Fields controlled the geological and geomorphological evolution of this coastal sector (Figure 1b). Caldera forming eruptions produced typical circular landforms and buried normal fault zones. In addition, eustatic sea-level fluctuations modified the coastline leading to lacustrine and palustrine environments in the coastal plain [58].

From a geological point of view, the *Cumae* archaeological site is located directly adjacent to the western edge of the Campanian Ignimbrite (CI) caldera, dated 39 ka BP [59] (Figure 1a,b). Several buried normal faults, fractures and deep crater rims characterize this sector of the Phlegraean Fields. The study site is characterized by a complex coastal volcanoclastic-sedimentary sequence, formed by sandy silts, silts, clays and peats of marine, alluvial and lagoon–palustrine environments, laterally passing into aeolic sands next to the shoreline [60,61]. This sedimentary coastal complex has unconsolidated ash-fall pyroclastic deposits formed by fine ashes and pumices and consolidated yellow tuffs. The transition from a volcanic to coastal environment produced a strong lithostratigraphic heterogeneity (Figures 1b and 2a,b).

The local geomorphology is typical of a coastal plain, with altitudes between 0 and 16 m a.s.l. (Figure 1c). From the sea toward the inland area, the site is characterized by a dune system and a wetland in the retro-dunal zone (Figure 1c). The Cuma Mount, a 85 m a.s.l. high remnant of a pre-CI volcanic building older than 39 ka [61], rises from the flat morphology of the coastal plain (Figure 1b,c).

From the hydrogeological point of view, the groundwater flow system is unitary (Figure 1b) at the basin scale [62,63], although it is locally influenced by hydraulic heterogeneity of volcano-sedimentary succession, groundwater pumping and reclamation drainage channel system. The hydrogeological basin which includes the study site (Figure 1b) extends for about 1.7 km<sup>2</sup> with a groundwater flow oriented toward the coastline in the west (Figure 1b). It is characterized by a grade of vulnerability to pollution from medium to high [64]. At the small scale, the study site hosts a porous multilayered aquifer system (Figure 2a,b) formed by a shallow phreatic aquifer in the pyroclastic and pyroclastic-alluvial-lacustrine sediments (pyroclastic (P) and pyroclastic-alluvial-lacustrine (PAP) complexes) and a semiconfined deep aquifer in the older pyroclastic deposits (DPs complex), separated by a deka-m thick lithic tuffaceous aquitard (YT). In the coastal zone, this YT aquitard is absent resulting in one single unconfined shallow aquifer (Figure 3a), hosted in the dune complex [65].



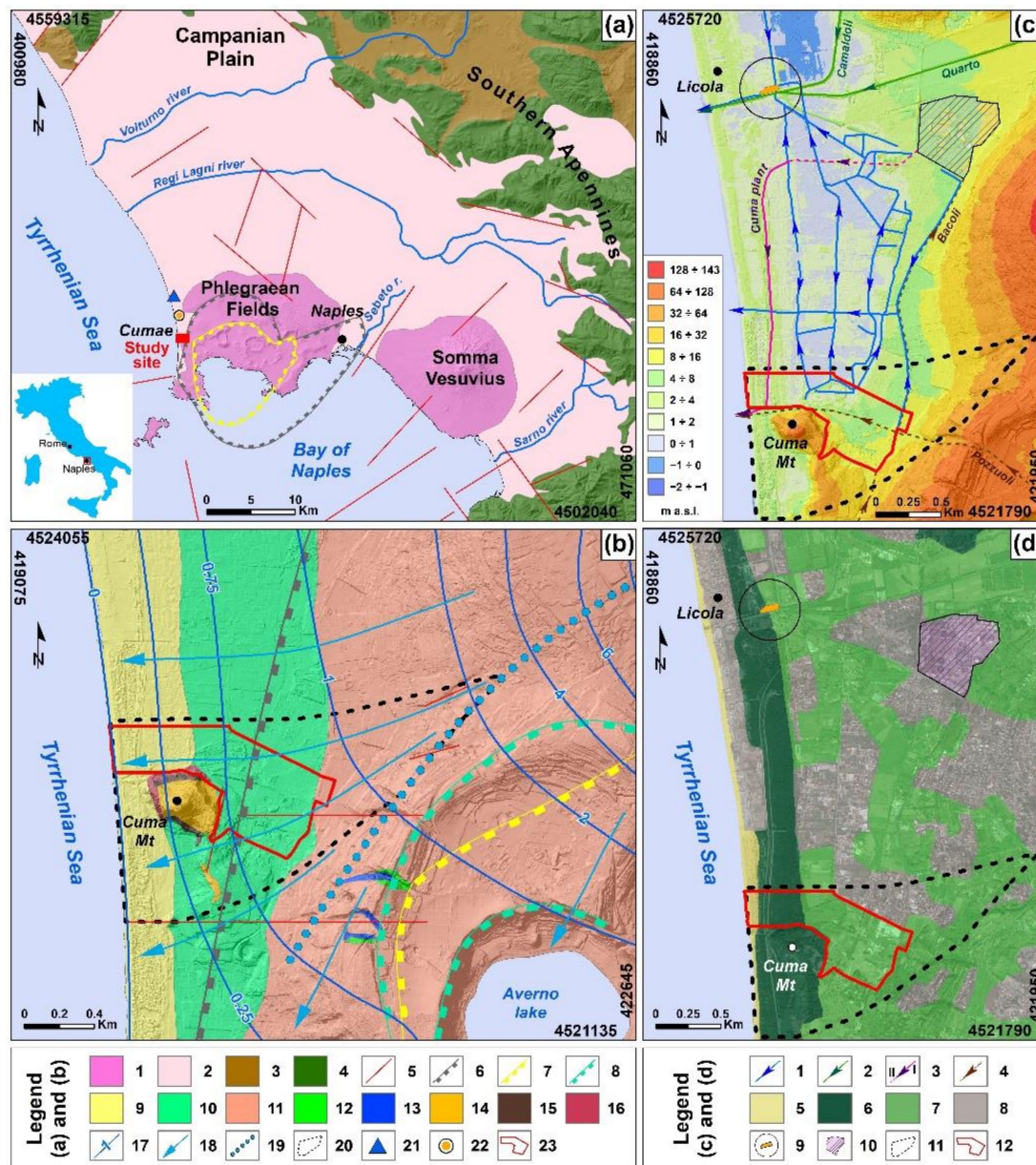


**Figure 1.** (a) Geological map of Campanian Plain and (b) hydrogeological map of the eastern sector of Phlegraean Fields (after [61] modified). Legend: (1) Quaternary epiclastic deposits; (2) Quaternary volcanic deposits; (3) Miocene deposits; (4) Mesozoic Apennine platform carbonates; (5) buried fault; (6) Campanian Ignimbrite (CI) caldera boundary; (7) Neapolitan Yellow Tuff (NYT) caldera boundary; (8) buried caldera boundary; (9) Eolic deposits; (10) Pyroclastic-fluvio-palustrine deposits; (11) Pyroclastic deposits; (12) Baia's tuffs; (13) Gauro's eruption deposits; (14) Neapolitan Yellow Tuff; (15) Museum Breccia; (16) Cuma Mt lavas; (17) groundwater contour line (m a.s.l.); (18) groundwater flow direction; (19) groundwater divide; (20) hydrogeological basin of study area; (21) Licola pluviometric station; (22) Licola draining station; (23) study area. (c) Geomorphological setting, hydrographic network and (d) land use of the hydrographic and hydrogeological basin of study area. (1) Reclamation draining channel; (2) surface water channel; (3) open-air (i) and underground (ii) Cuma wastewater treatment plant discharge channel; (4) underground wastewater channel; (5) beach; (6) Mediterranean bush and pinewood; (7) agricultural land; (8) urban area; (9) Licola drainage station; (10) Cuma wastewater treatment plant; (11) hydrogeological basin of study area; (12) study area.



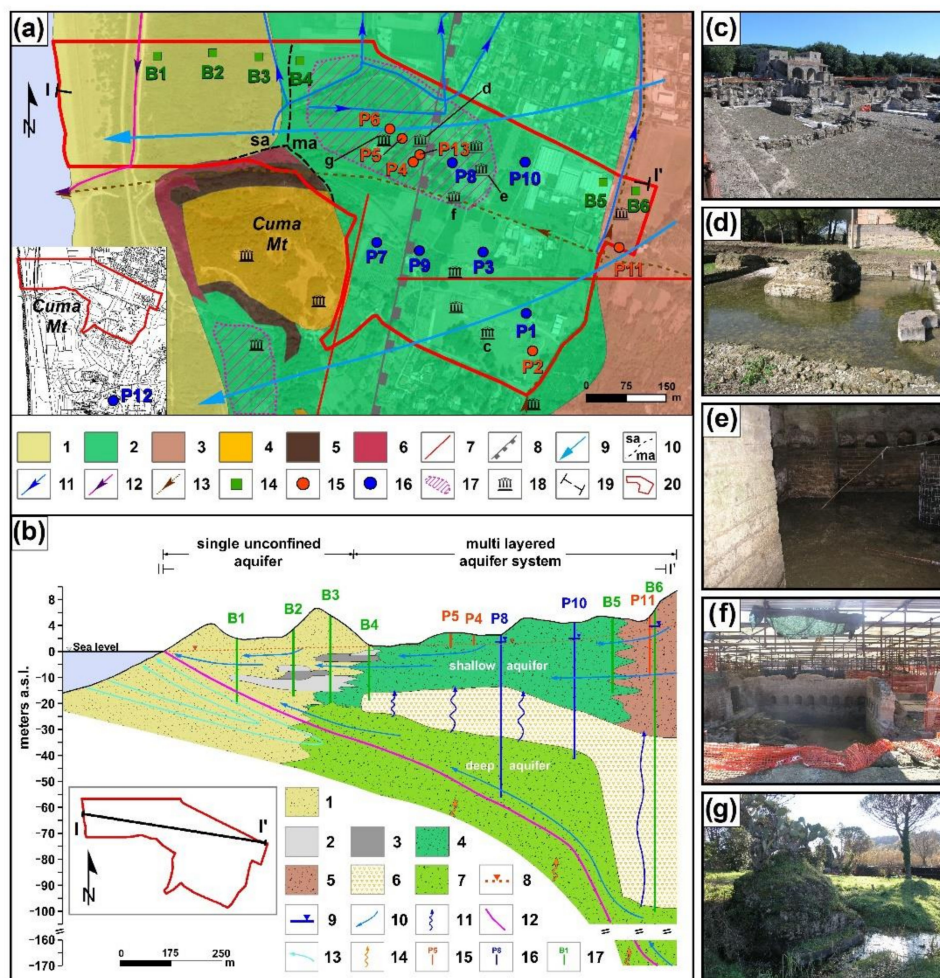


**Figure 2.** (a) Geological map of study area and hydrogeological monitoring network. Legend: (1) Eolian deposits; (2) Pyroclastic-fluvio-palustrine deposits; (3) Pyroclastic deposits; (4) NYT; (5) Museum Breccia formation; (6) Cuma Mt lavas; (7) buried fault; (8) CI caldera boundary; (9) groundwater flow direction; (10) single unconfined aquifer (sa) and multilayered aquifer system (ma) sectors; (11) groundwater draining channel; (12) Cuma plant discharge channel; (13) underground wastewater channel; (14) borehole; (15) shallow well; (16) deep well; (17) groundwater flooding (GF) area; (18) archaeological site of Necropolis (GF impacted in (d–g)); (19) trace of hydrostratigraphic section; (20) study area. (b) 2D hydrostratigraphic model of the aquifer system. (1) Dune complex; (2) silts; (3) clays and peaty deposits; (4) pyroclastic-alluvial-lacustrine (PAP) complex; (5) pyroclastic (P) complex; (6) tuffaceous aquitard (YT) aquitard; (7) pyroclastic deposits (DPs) complex; (8) piezometric level of shallow unconfined aquifer; (9) piezometric level of deep semiconfined aquifer; (10) groundwater flow direction; (11) vertical groundwater flow direction; (12) Fw-Sw interface; (13) saline groundwater flow; (14) high mineralized fluids rising; (15) shallow well; (16) deep well; (17) borehole.

The surface hydrography is controlled by a reclamation drainage system of micro-channels, which locally crosses the whole retro-dunal zone of the coastal plain and whose altitude is very close to the sea level or just below it (Figure 1c). It was built during the last two centuries, draining surface and groundwater either to the sea directly or through the Licola mechanical pumping station. In addition, open-air and underground channels carry wastewater to the Cuma wastewater treatment plant and to the sea (Figures 1c and 2a).

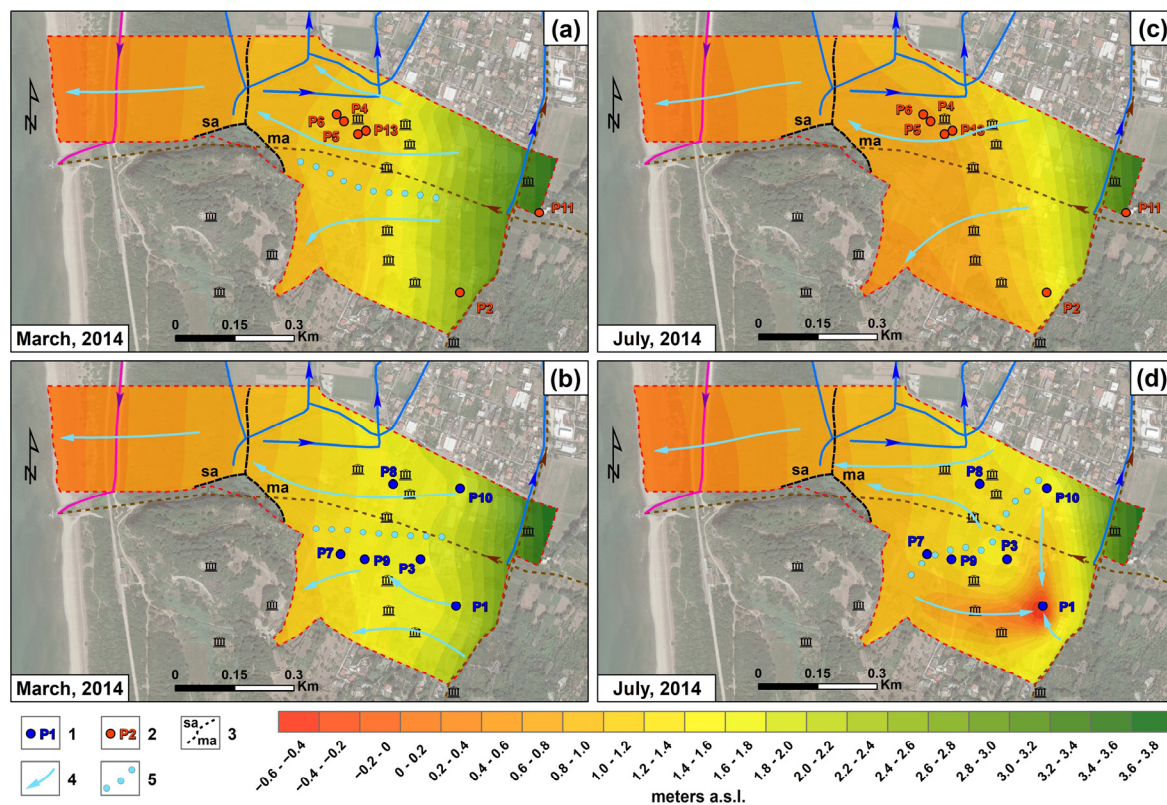


**Figure 3.** Groundwater flow pattern in March 2014 (a,b) and July 2014 (c,d) for the shallow (a,c) and deep (b,d) aquifer. Legend: (1) Deep well; (2) shallow well; (3) hydrogeological limit between the single phreatic (sa) and the multilayered (ma) aquifer; (4) groundwater flow direction; (5) groundwater divide.

Land use consists prevalently of agricultural lands, corresponding to about 70% of the study area (Figure 1d), in which intensive cultivation is practiced by applying pesticides and chemical and organic fertilizers. About 30% is covered by Mediterranean bush and pinewood ending with a narrow stretch of beach. Moreover, within the hydrogeological basin, sparsely urban areas are present, which are partially covered by a sewage network and, where it is locally absent, septic tanks are used. The climate is of Mediterranean type, characterized by hot dry summers and moderately cool and rainy winters. The range of mean annual air temperatures is approximately 13–15 °C and the average annual rainfall is about 700 mm/year [66].

Finally, in the last two decades, the study area has been recognized as affected by hydro-environmental criticalities which endanger the state of conservation of artefacts, cultural remains and ancient monuments of the *Cumae* archaeological site (Figure 2a,d–g). Indeed, as observed in other sectors of the Metropolitan City of Naples [50,51,67,68], the rising of groundwater level and related Groundwater Flooding (GF) phenomena have been registered, causing damage to structural and decorative features of buried archaeological artefacts. Both hydrological processes are mainly attributed to the rising of sea levels from the Roman period to the present in the central area of Mediterranean basin [69] and to local volcano-tectonic land subsidence [70]. Consequently, since the early 2000s numerous GF episodes, with groundwater levels up to +1.20 m at the base of some archaeological remains, have been observed in the retro-dunal zone, at the Monumental Roman Necropolis of the *Cumae* archaeological site (Figure 2a,e–g), despite the local presence of a man-made micro-channel reclamation drainage system (Figure 2a).

### 3. Materials and Methods

Eleven field campaigns were carried out from December 2013 to February 2015. Water table level was monitored and groundwater samples were collected in thirteen domestic and agricultural wells:



6 shallows wells (P2, P4, P5, P6, P11, P13, up to 15 m depth, Figure 2a) and 7 deep wells (P1, P3, P7, P8, P9, P10, P12 up to 80 m depth, Figure 2a) on a monthly frequency. The wells P1, P3, P7, P8, P10 and P12 were equipped with submersible pumps used for purging and sampling while the wells P2, P4, P5, P6, P9, P11, and P13 were sampled by bailer, after rinsing it three times with sample water.

Physico-chemical parameters (i.e., temperature, pH, electrical conductivity, alkalinity) were measured by field analysis. Hydrochemistry (i.e., major ions and trace elements), isotopic ratios (i.e.,  $\delta^{18}\text{O}$  and  $\delta\text{D}$  in water,  $\delta^{15}\text{N}\text{--NO}_3$  and  $\delta^{18}\text{O}\text{--NO}_3$ ,  $\delta^{11}\text{B}$ ) and  $^{222}\text{Rn}$  specific activity was determined in groundwater samples in the laboratory. Results of hydrogeological, hydrochemical, and isotopic monitoring are listed in Table S1 in the supplementary materials.

### 3.1. Hydrogeological Survey

In order to analyze groundwater flow and the spatio-temporal variation of the piezometric levels, a groundwater monitoring network was reconstructed inside the *Cumae* archaeological park (Figure 2a). The piezometric levels were monitored monthly from December 2013 to February 2015 in 6 shallow wells (P2, P4, P5, P6, P11, P13, up to 15 m depth) and in 7 deep-wells (P1, P3, P7, P8, P9, P10, P12 up to 80 m depth). Monitoring was performed by a water level meter (BFK-100 model, PASI, Italy). The ground elevation of the wells was measured by the DGPS technique (K9 Series RTK, KOLIDA Instrument, China) and verified through the reconstruction of a Digital Elevation Model (DEM) derived from a LiDAR survey [71] with  $1 \times 1 \text{ m}^2$  cells, implemented in a GIS environment. Multitemporal maps of groundwater table elevations were constructed for both the shallow and the deep aquifers, through the Triangulated Irregular Network (TIN) interpolation method applied to the piezometric levels in March and July 2014, representative of recharge (Rc) and recession (Rs) periods, respectively. Daily pluviometric time series were recorded by Regional Civil Protection at the Licola (Naples, Italy) gauge station (Figure 1a).

### 3.2. Hydrochemical Sampling and Analysis

Physico-chemical parameters as pH, electrical conductivity (Electrical conductivity (EC),  $\mu\text{S}/\text{cm}$ ) and temperature ( $T$ ,  $^{\circ}\text{C}$ ) were measured in situ by a multiparametric probe (Mod. Sea Bird Electronics 911 Plus CTD; Sea-Bird Electronics). Alkalinity was determined in the laboratory by a titrimetric method.

In order to determine major anions and cations (i.e.,  $\text{HCO}_3^-$ ,  $\text{SO}_4^{2-}$ ,  $\text{Cl}^-$ ,  $\text{Br}^-$ ,  $\text{F}^-$ ,  $\text{Ca}^{2+}$ ,  $\text{Mg}^{2+}$ ,  $\text{Na}^+$ ,  $\text{K}^+$ ) and trace elements (i.e., As, B, etc.), water samples were collected in 1 L high-density polyethylene (HDPE) bottles avoiding air bubbles and stored at  $+4^{\circ}\text{C}$ . The samples for trace elements determinations were filtered ( $0.45 \mu\text{m}$ ) and acidified in the field. Anions and cations were determined by ion chromatography (IC Metrohm 850 Professional). Cations were separated by a Metrosep C4 250/4.0 column using 3.0 mM  $\text{HNO}_3$  as eluent and a flow rate of 0.9 mL/min, whereas anions were separated by a Metrosep A supp7 250/40 column using 3.6 mM  $\text{Na}_2\text{CO}_3$  as eluent at a flow rate of 0.7 mL/min. The accuracy of the analyses was checked by the ionic balance; analyses with an ionic balance within  $\pm 5\%$  range were considered acceptable. For trace element determinations, the filtered samples were acidified with a 3% *v/v*  $\text{HNO}_3$  solution and analyzed by inductively coupled plasma with mass spectrometry (ICP-MS, Aurora M90, Bruker Daltonics, Billerica, MA, USA). Hydrochemical analyses were conducted at the Chemical Science Department, University of Naples Federico II.

### 3.3. Isotopic Monitoring

Water samples for  $^{222}\text{Rn}$  determinations were sampled by means of a 10 mL plastic syringe, avoiding contact with air according to the sampling procedure suggested by the U.S. Environmental Protection Agency (US EPA) [72] and modified by Belloni et al. [73] to perform liquid scintillation counting (LSC) measurements and were analyzed at least 3 h after the collection to allow equilibrium to be reached between  $^{222}\text{Rn}$  and its daughters; counting time was 15 min; blank samples and a certified  $^{226}\text{Ra}$  reference sample were counted together with the water samples at every counting session at the Center for Isotopic Research on Cultural and Environmental heritage (CIRCE) of the Department



of Mathematics and Physics, University of Campania “Luigi Vanvitelli” (San Nicola la Strada, Italy). The lower detectable level was 0.5 Bq/L. Three replicates were sampled at each site.

Water samples for  $\delta^{18}\text{O}$  and  $\delta\text{D}$  analyses were collected in 50 mL narrow neck HDPE bottles, leaving no headspace to avoid contact with air and horizontally stored at 4 °C [74].  $\delta^{18}\text{O}$  and  $\delta\text{D}$  isotopic ratios of 0.45  $\mu\text{m}$  filtered samples, reported as permil (‰) relative to Vienna Standard Mean Ocean Water, were analyzed by a TC/EA-ConFloIII-IRMS system (DeltaV, Thermo Fisher) at CIRCE. The precision of the measurements was 0.1‰ and 1‰ for  $\delta^{18}\text{O}$  and  $\delta\text{D}$ , respectively.

$\delta^{15}\text{N}$  and  $\delta^{18}\text{O}$  of dissolved nitrate, reported as permil (‰) vs. AIR and VSMOW, respectively, were measured in groundwater samples by means of the silver nitrate method [75] and analyzed by a TC/EA-ConFloIII-IRMS system (Delta V, Thermo Fisher, Waltham, MA, USA) CIRCE. The precision of the whole procedure involving the preparation protocol of aqueous samples, reference materials and the IRMS analysis of solid  $\text{AgNO}_3$  salt was 0.7‰ and 1.2‰ for  $\delta^{15}\text{N}$  and  $\delta^{18}\text{O}$ , respectively.

Water samples for  $\delta^{11}\text{B}$  determination were collected in two shallow wells (P5 and P11) and in five deep wells (P1, P3, P7, P8, P10) in April (recharge phase) and July (recession phase) 2014 in 1000 mL narrow neck HDPE bottles, leaving no headspace to avoid contact with air and stored at room temperature. The chemical procedure for boron isotope measurement was based on the GAMA method [76]: all samples were filtered on nylon membrane filters (0.45  $\mu\text{m}$ ) to remove particles and loaded on a boron-specific ion exchange resin, Amberlite IRA743 [77,78]. In each procedural batch, about 20 boron samples, blanks (1 machine plus 1 procedural), 1 boric acid reference material (NIST SRM951: 1 processed and 1 unprocessed), and 1 internal boric acid standard as a Quality Check (QC) were prepared loading about 50  $\mu\text{g}$  of dissolved boron onto the resin. Boron isotopic measurements were performed by a Thermo Fisher Scientific Neptune Plus (High Resolution Multicollector) ICP-MS at the CIRCE (Centre for Isotopic Research on Cultural and Environmental heritage) laboratory, Dept. of Mathematics and Physics, University of Campania “Luigi Vanvitelli” (Caserta, Italy). The analysis procedure involved data calibration through procedural reference materials (SRM951) and internal standards measurements applying Quality Assurance (QA) rules. The instrumental precision was about 0.15‰ for signals  $>1$  V.

$^{222}\text{Rn}$  specific activity in groundwater was measured to infer information about aquifer heterogeneity and deep fluid rise to the surface. The stable isotopes of the water molecule,  $^{18}\text{O}$  and  $^2\text{H}$ , were used to study groundwater origin, recharge and mixing processes since they are incorporated within the water molecule and are hydrologically conservative. Nitrogen and Oxygen isotopic ratios of dissolved nitrate and isotopic ratios of Boron stable isotopes were studied to identify possible groundwater contamination sources and their attenuation processes as well as groundwater origin.

## 4. Results

Maps of groundwater flow and spatial distributions of the physico-chemical parameters were carried out, for March 2014 and July 2014, considering representative of recharge (Rc) and recession (Rs) hydrological periods, respectively. The temporal variation of each analyzed parameter was reported in box plot diagrams of the shallow and deep wells for each campaign. In addition, cross-plots of molar ratios and isotopes allowed us to identify clusters in samples and sources of groundwater contamination and salinization.

Results were interpreted to implement a conceptual hydrogeological–hydrogeochemical model of the study area, highlighting the natural and anthropogenic processes influencing the hydrochemical characteristics of the volcano-sedimentary aquifer.

### 4.1. Hydrogeology

Figure 3 shows the piezometric maps of the shallow and the deep aquifers in the Rc and Rs periods.

The shallow phreatic aquifer flows in the pyroclastic (P), pyroclastic-alluvial-lacustrine (PAP), and Dune complexes (Figure 2b) with a generalized W–E orientation. In the central sector, a groundwater divide splits the flow in a northern and a southern circulation in correspondence with the volcanic relief

of Cuma Mt. Piezometric heads in shallow piezometers varied between 0 and 3.68 m a.s.l. with a mean gradient of about  $3.0 \times 10^{-3}$  in March 2014 (Figure 3a), and between 0 and 3.58 m a.s.l. with a mean gradient of about  $2.9 \times 10^{-3}$  in July 2014 (Figure 3c). The difference between the level maximum during the recharge period (March) and level minimum during the dry season (July) is 0.1 m. Piezometric contour maps show a similar pattern in both considered periods. Nevertheless, minor local differences are observed in the retro-dunal zone. During recharge, highest water table elevation is reached, and the reclamation micro-channel system partially drains groundwater (Figure 3a). This evidence is not registered during the Rs period (Figure 3c), in which the piezometric levels are below the channel base not influencing groundwater flow. No influence on the Pozzuoli and Bacoli underground wastewater channels that pass through the study area (Figures 1c and 2a) on the piezometric contours (Figure 1a,c) was observed.

The deep aquifer flows into the DP complex under semiconfined condition, and then joins the shallow aquifer in the coastal Dune complex, where lithic tuffaceous aquitard (YT) is absent. In March 2014 (Figure 3b), groundwater flow was oriented W–E with a split due to the Mt. Cuma solid rock basement, similarly to what happens for the shallow aquifer. Piezometric levels ranged between 0 and 3.82 m a.s.l. with a gradient of  $2.8 \times 10^{-3}$ . In the vegetation period, the deep aquifer was affected by abstraction for irrigation and a significant depression of hydraulic heads—down to  $-2.3$  m a.s.l. in early October 2014 in well P3 (Table S1) and to  $-0.76$  m a.s.l. in July 2014 in well P1 (Table S1 and Figure 3d).

Median values of piezometric levels (PLs) measured in shallow wells were quite constant for the whole monitoring period with a maximum variation of 0.34 m (1.16 m in April and 0.82 m in July 2014) (Table S1). Median values of PLs measured in deep wells are generally higher than those in shallow wells throughout the monitoring year, indicating an upward flow which is inverted only during the Rs, when pumping induces a sharp decrease in PLs (e.g., P1 and P3).

The comparison between the piezometric levels observed in the two seasons shows that the deep aquifer has higher hydraulic head in the Rc period, causing an upwards oriented vertical flow recharging the shallow aquifer. This relation is locally reversed in the Rs period, when pumping draws the deep aquifer down.

#### 4.2. Hydrochemistry

Physical and chemical parameters determined for groundwater samples taken from the monitoring network (Figure 2) are listed in Table S1.

Hydrochemical facies of samples were identified by a Langelier–Ludwig diagram [79] and mapped for Rc and Rs periods. Physico-chemical parameter values (electrical conductivity, EC, and temperature, T) and concentration of major ions and trace elements ( $[\text{SO}_4^{2-}]$ ,  $[\text{Cl}^-]$ ,  $[\text{F}^-]$ ,  $[\text{NO}_3^-]$ , [As] and [B]) were plotted in box-plot diagrams considering separately all shallow and deep wells for each campaign, in order to analyze their temporal variation. The same parameters and analytes were mapped through bubbles sized proportionally to their value or concentration for the month of March and July 2014, in order to analyze their spatial distribution and to highlight local anomalies. In addition, cross-plots of molar ratios, in detail  $r[\text{SO}_4/\text{Cl}]$  vs.  $[\text{Cl}]$ ,  $r[\text{Mg}/\text{Cl}]$  vs.  $r[\text{Br}/\text{Cl}]$ ,  $r[\text{B}/\text{Cl}]$  vs. [B] and  $r[\text{B}/\text{Cl}]$  vs.  $r[\text{Br}/\text{Cl}]$ , were represented to identify sample clusters and to compare their trend with the sources values (i.e., agricultural drainage, sewage, hydrothermal waters, etc.) [10].

Groundwater of shallow and deep aquifers prevalently belong to the NaK-ClSO<sub>4</sub> type both in the Rc and Rs periods, as shown in the Langelier–Ludwig diagram [79] (Figure 4). Exceptions are represented by P1 and P3 agricultural deep wells, which belong to CaMg-ClSO<sub>4</sub> and CaMg-HCO<sub>3</sub> types in the Rc period, respectively. Because they are affected by pumping, their hydrochemical facies (temporarily) change toward the NaK-ClSO<sub>4</sub> type, along the geothermal and seawater–groundwater mixing lines, indicating advection from the freshwater seawater interface.

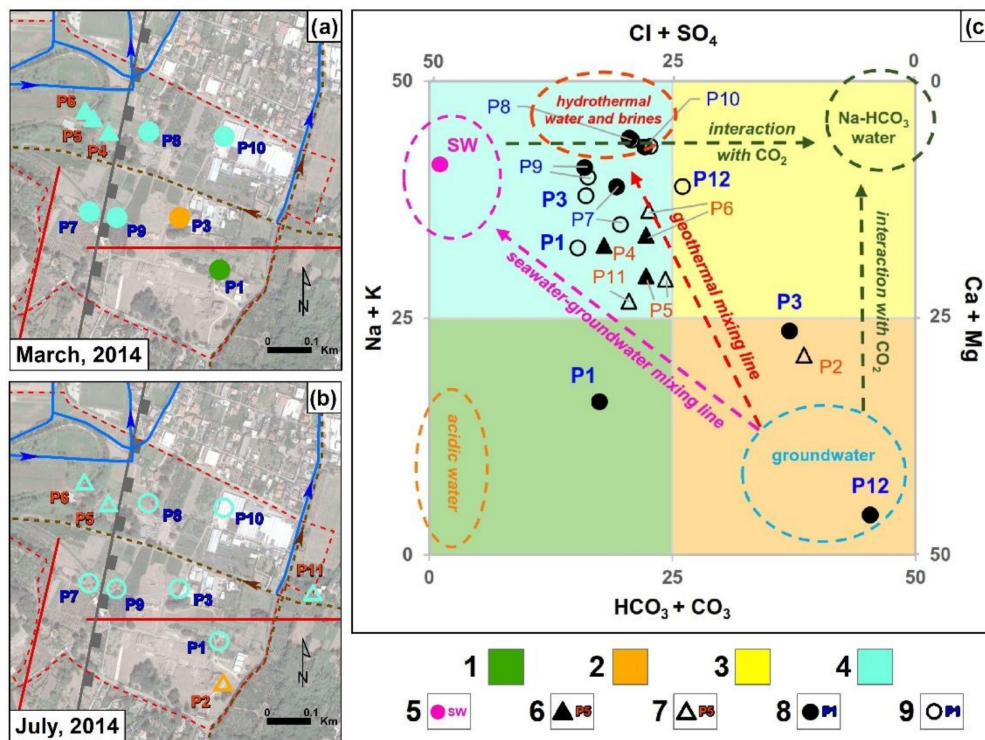


**Figure 4.** Spatial distribution of hydrochemical facies of shallow and deep wells, for the period (a) March 2014 and (b) July 2014, and (c) Langelier–Ludwig diagram. Legend: (1) CaMg- $\text{ClSO}_4$  type; (2) CaMg- $\text{HCO}_3$  type; (3) NaK- $\text{HCO}_3$  type; (4) NaK- $\text{ClSO}_4$  type; (5) sea water; (6) shallow wells in March 2014; (7) shallow wells in July 2014; (8) deep wells in March 2014; (9) deep wells in July 2014.

The spatial and the temporal distribution of selected physical and chemical parameters are reported in Figures 5 and 6. In Figure 5, box plots of climatic, hydrogeological and hydrogeochemical parameters for the whole monitoring period, with indication of the recharge (Rc), depletion (Rs), fertilization (Ft) and pumping (Gp) phases. The parameters are rainfall in mm and air temperature, groundwater level, groundwater temperature, EC,  $[\text{NO}_3^-]$ ,  $[\text{SO}_4^{2-}]$ ,  $[\text{Cl}^-]$ ,  $^{222}\text{Rn}$  specific activity,  $[\text{F}^-]$ ,  $[\text{As}]$ ,  $\delta^{18}\text{O}$ . In Figure 6 the spatial distribution of the selected parameters is represented for Rc and the Rs in shallow and deep wells by means of bubbles with the radius proportional to parameter values.

Groundwater temperature presents slight differences between the shallow and the deep aquifers. The groundwater temperature trend (Figure 5a,c) mirrors that of the air temperature, even if the shallow wells show a wider range of variation (between 9.0 °C in December 2014 and 25.9 °C in June 2014) with respect to the deep ones (between 14.2 °C in December 2014 and 25.5 °C in July 2014). This indicates that groundwater temperature of the shallow phreatic aquifer is more influenced by air temperature than the deep semiconfined aquifer. The spatial distribution of groundwater temperature confirms the minor differences between the two aquifers in the Rc and Rs periods (Figure 6a,b).



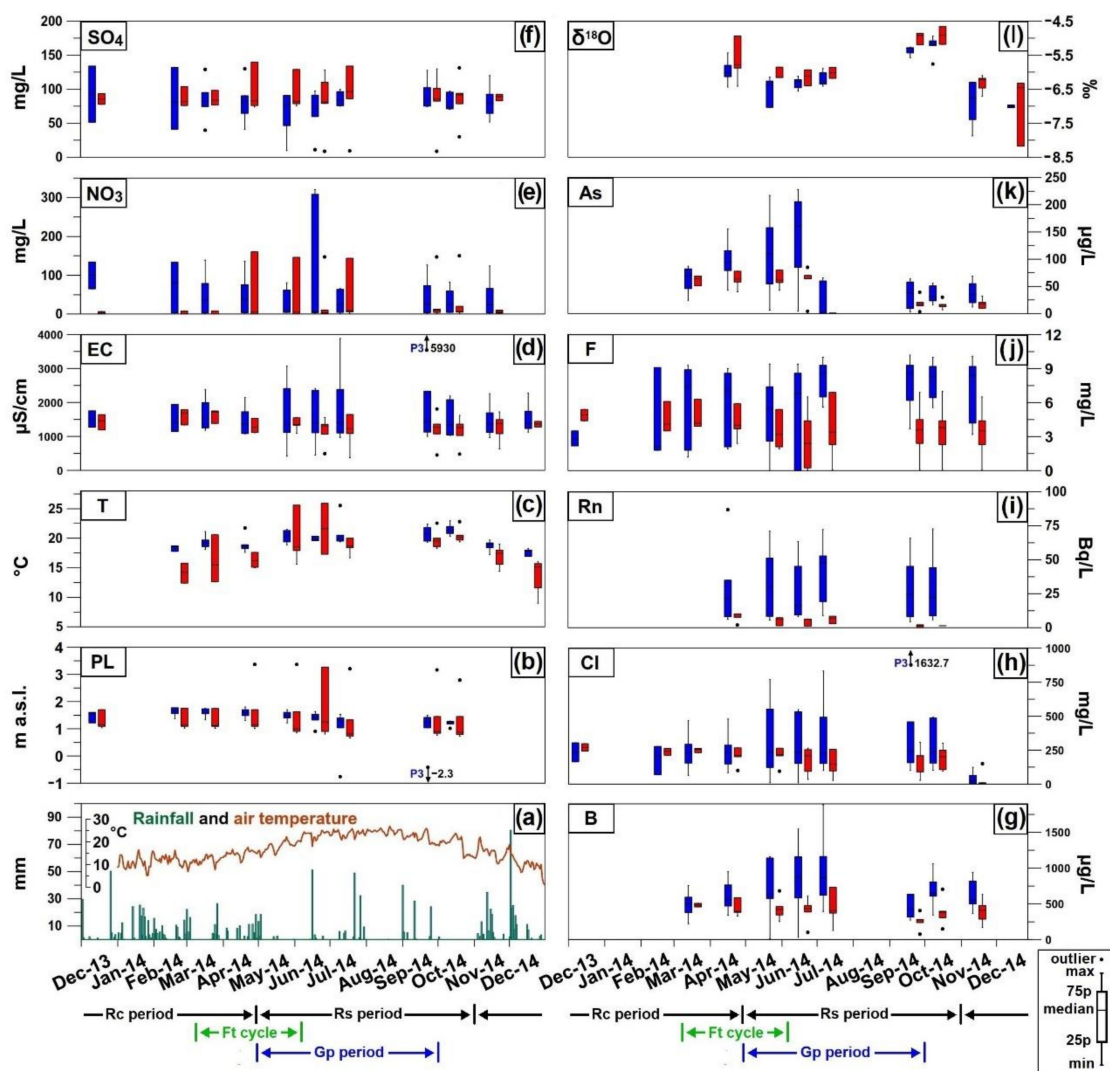


**Figure 5.** Box plots of climatic, hydrogeological, and hydrogeochemical parameters for the whole monitoring period, with indication of recharge (Rc), recession (Rs), fertilization (Ft) and pumping (Gp) phases; (a) rainfall and air temperature; (b) piezometric levels; (c) groundwater temperature; (d) electric conductivity; (e) concentration of  $\text{NO}_3^-$ , (f)  $\text{SO}_4^{2-}$ , (g) B, (h)  $\text{Cl}^-$ , (i)  $^{222}\text{Rn}$ , (j)  $\text{F}^-$ , (k) As and (l)  $\delta^{18}\text{O}$  isotopic ratios. Box plots represent the distributions measured in shallow (red) and deep (blue) piezometers.

Electrical conductivity (EC) remains almost constant during the whole monitoring period (Figure 5d). Minimum values are slightly higher for the deep aquifer (423  $\mu\text{S}/\text{cm}$  compared to 375  $\mu\text{S}/\text{cm}$  of shallow aquifer), and maximum values show strong differences locally (Figure 6c,d). In fact, P1 and P3 wells register maximum values during the Rs period (EC up to 5930  $\mu\text{S}/\text{cm}$  reached in P3 in early October 2014; showed in Figure 5d), in which they are affected by pumping and characterized by the lowest piezometric levels, highlighting a significant increase compared to the Rc period (Figure 6c,d), as already showed in Section 4.1 for P1 and P3.

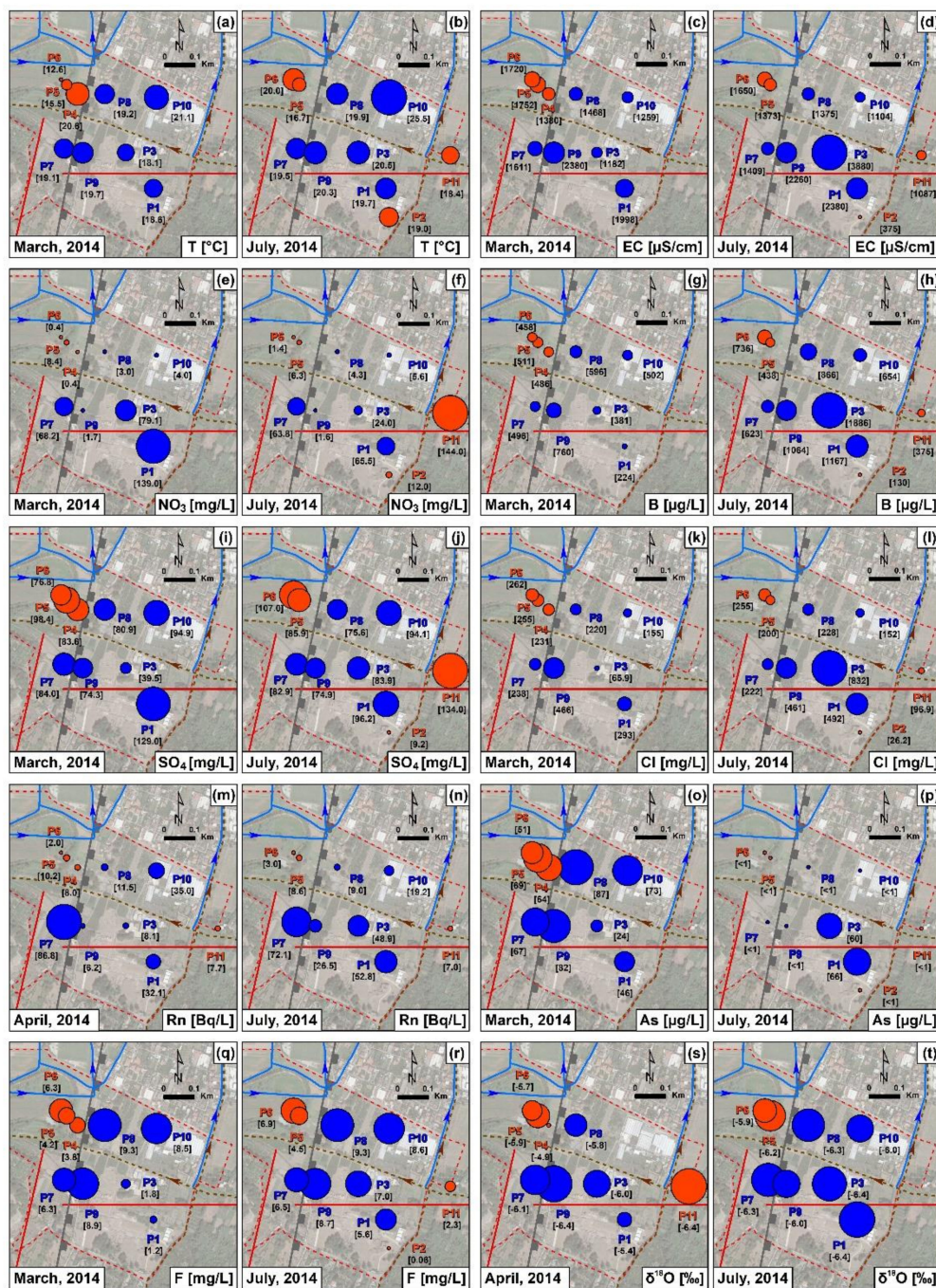


**Figure 6.** Bubble maps of values of physico-chemical parameters (T (a) and (b) and -EC (c) and (d)), concentrations of major ions and trace elements ( $\text{NO}_3^-$  (e) and (f), Boron (g) and (h),  $\text{SO}_4^{2-}$  (i) and (j),  $\text{Cl}^-$  (k) and (l),  $\text{F}^-$  (q) and (r) and Arsenic (o) and (p)) and isotopes ( $^{222}\text{Rn}$  (m) and (n) and  $\delta^{18}\text{O}$  (s) and (t)) in Rc and Rs periods for the shallow (in red) and deep (in blue) wells. Radius of bubbles is proportional to the value of each parameter.

The concentrations of major ions and trace elements, indicators of contamination sources and interactions between groundwater and deep fluids, show higher average concentrations in deep wells, consistently. This can be observed in the concentrations of  $\text{Cl}^-$  (Figures 5h and 6k,l),  $\text{F}^-$  (Figures 5j and 6q,r), Boron (Figures 5g and 6g,h), Arsenic (Figures 5k and 6o,p) and  $^{222}\text{Rn}$  (Figures 5i and 6m,n). As previously shown for the EC, P1 and P3 deep wells present consistent differences also in the concentration of the above solutes. In detail, they have lower concentrations



than the other deep wells in the Rc period. In the Rs period, P1 and P3 are affected by pumping and fluorides increase up to 5.6 and 7.0 mg/L, respectively, approaching the mean of the other deep wells (8.3 mg/L); Boron (1167 and 1888 µg/L),  $\text{Cl}^-$  (492 and 832 mg/L) and Arsenic (66 and 60 µg/L) reach the highest concentrations. (Table S1).

During the whole monitoring, nitrate concentrations present high values in the deep wells (Figures 5e and 6e,f), with a median value of 82.4 mg/L compared to only 6.3 mg/L in shallow wells. Nevertheless, maximum values are registered in P11, an agricultural shallow well (Figure 6f), which reaches a concentration above 140 mg/L in the Rs period. A similar behavior was observed regarding sulphate (Figure 6i,j), where the highest concentration was measured in the P11 agricultural well ( $\geq 130$  mg/L in Rs period). High sulphate concentrations were almost homogeneously distributed both in shallow and deep wells (Figure 5f).

In synthesis, major ions and trace elements highlight significant differences between shallow and deep wells showing recurring site-specific behaviors. Among shallow wells, two main areas can be identified along groundwater flow from upstream wells (P11 and P2, Figures 3 and 7) characterized by lower chloride and boron concentrations and higher sulphate concentrations at a sub-zero sea level, i.e., a temporarily submerged area, where the drainage system catches groundwater diffuse outflow (wells P4, P5, P6 and P13; Figure 7a,c), which is characterized by higher concentrations of solutes, likely influenced by the mixing with mineralized groundwater upwelling (Figure 7a). P11 shows  $[\text{SO}_4^{2-}] > 1$  meq/L (equivalent about 50 mg/L), likely due to fertilizer leaching, as  $[\text{NO}_3^-]$  also suggests (annual average:  $2.4 \pm 0.1$  meq/L, equivalent to about 150 mg/L) (Table S1 and Figure 6e,f). The deep wells show very variable solute concentrations and, in particular, upstream wells (P10 and P12, Figures 3 and 7) are characterized by lower values of chloride and boron (Figure 7a,c) while higher values are found in the P1, P7, P8 and P9 wells and in P3 in the abstraction phase which promotes the rise of mineralized groundwater.

In Figure 7b, the molar ratio of  $[\text{Mg}/\text{Cl}]$  is reported vs.  $r[\text{Br}/\text{Cl}]$  to show the origin of shallow and deep groundwater. The molar ratios show a narrow range of variation for shallow groundwater while deep groundwater is characterized by a greater dispersion of the  $r[\text{Mg}/\text{Cl}]$  values. They are far below the ratio of seawater, making a mixing with hydrothermal waters and a small or null interaction with seawater likely [80]. Similar trends are highlighted in Figure 7c where  $r[\text{B}/\text{Cl}]$  vs.  $[\text{B}]$  is plotted with  $[\text{As}]$  as an additional independent variable, as a tracer of groundwater affected by hydrothermal fluids in the volcanic region [81]. In general, all the wells (except P1 and P3) are characterized by a linear relation between  $r[\text{B}/\text{Cl}]$  and  $[\text{B}]$ , covering a wide range of mineralization conditions showed by the different slopes (i.e.,  $r[\text{B}/\text{Cl}]/[\text{B}]$ ). In particular, the shallow wells group into two main areas: an upstream (wells P2 and P11) and a central area corresponding to the retrodunal depression where flooding is observed (Figure 2a; wells P4, P5, P6 and P13)—both characterized by  $[\text{As}] < 100$  µg/L. On the contrary, deep wells (P1, P8, P9 and P10) are characterized by higher  $[\text{As}]$  in the recharge period and a variable mineralization, which is higher in the drawdown period (Table S1). It is worth noting the behavior of well P3, which has low  $[\text{As}]$  both in the recharge and the recession periods, while  $r[\text{B}/\text{Cl}]$  significantly decreases in the recession periods indicating a mixing with more mineralized water. Well P12, upstream of the study area, is characterized by lower  $[\text{As}]$  and  $[\text{B}]$ , similar to the shallow P11 well. The hypothesis of a hydrothermal origin of the groundwater in the study area is further confirmed by the relation between  $r[\text{Br}/\text{Cl}]$  and  $r[\text{B}/\text{Cl}]$  reported in Figure 7d, where both shallow and deep groundwater fall into the box of the hydrothermal waters, characterized by  $r[\text{Br}/\text{Cl}]$  ranging from  $6 \times 10^{-4}$  and  $2 \times 10^{-3}$  and  $r[\text{B}/\text{Cl}]$  ranging from  $2.5 \times 10^{-3}$  and  $1 \times 10^{-1}$  [10]. Again, wells P1 and P3 in the recession period during pumping showing a trend toward lower  $r[\text{B}/\text{Cl}]$  values, suggesting mixing with more mineralized groundwater.



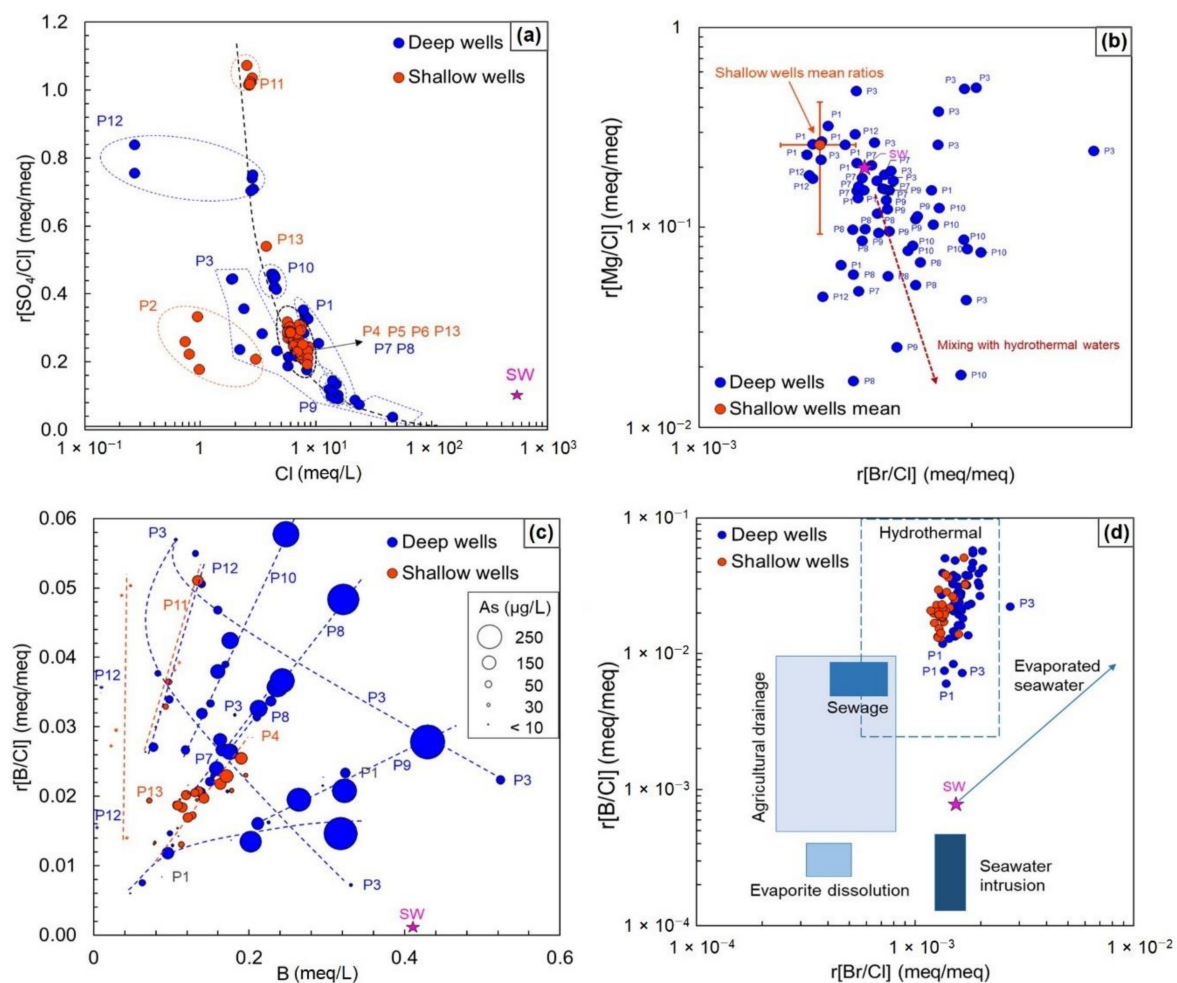


**Figure 7.** Plots of (a)  $r[\text{SO}_4/\text{Cl}]$  vs.  $[\text{Cl}]$ , (b)  $r[\text{Mg}/\text{Cl}]$  vs.  $r[\text{Br}/\text{Cl}]$ , (c)  $r[\text{B}/\text{Cl}]$  vs.  $[\text{B}]$  and (d)  $r[\text{B}/\text{Cl}]$  vs.  $r[\text{Br}/\text{Cl}]$  in shallow (red circles) and deep (blue circles) wells; the pink star represents seawater (SW). In (c), the area of the circles is proportional to  $[\text{As}]$  and the dashed lines represent trends of the values measured in each well. In (d), the boxes represent the sources values (i.e., agricultural drainage, sewage, hydrothermal waters, etc.) (after [10]).

#### 4.3. Isotopic Survey

Hydrological isotope data presented in this work refer to the shallow and deep aquifers explored during the 2014 monthly field campaigns. In Figure 8a, the dual isotope diagram  $\delta^{18}\text{O}$  vs.  $\delta\text{D}$  reports groundwater measured in shallow and deep wells during the recharge and the dry periods. A Local Meteoric Water Line (Mt. Vesuvius MWL, [82]) has been also reported as a reference for the study area samples and the Global MWL [83] and the East Mediterranean MWL [84] as a comparison. Usually, groundwater has a constant isotopic signature throughout a hydrological year, reflecting the mean isotopic composition of local precipitation. Nevertheless, in the study area there is a significant difference between the Rc and the Rs periods, the former presenting more depleted isotopic ratios (Figures 5l and 6s,t) in both deep and shallow wells. This significant difference indicates the presence of short travel time of groundwater from the area of recharge. In general, isotopic values of shallow and deep wells are quite homogeneous in each hydrological period showing no appreciable differences, likely due to a common origin of the recharge water. Nevertheless, during the depletion period, and in particular in the two campaigns of October 2014 (Table S1 and Figure 8a), both shallow and deep wells show an enrichment trend. The observed horizontal shift from the Mt. Vesuvius MWL toward more

enriched  $\delta^{18}\text{O}$  values is likely due to recharge by evaporated water or to a more evident mixing with hydrothermal waters due to the dry period [85–89].

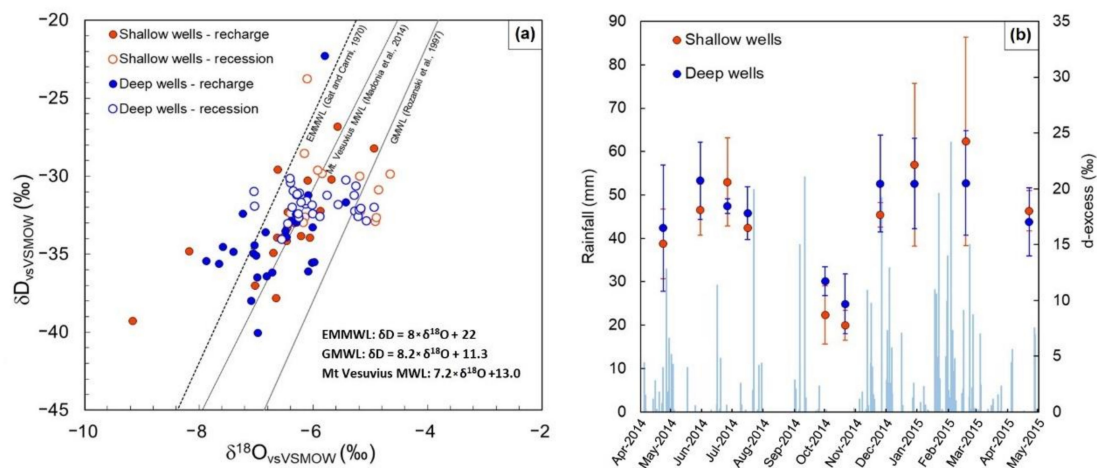


**Figure 8.** (a)  $\delta^{18}\text{O}$  vs.  $\delta\text{D}$  diagram in shallow and deep wells during the recharge (closed circles) and the depletion (open circles) hydrological phases in shallow (red circles) and deep (blue circles) wells. (b) Monthly variations of d-excess in shallow (red circles) and deep (blue circles) wells; the circles represent the mean values with 1 sigma standard deviation. In the plot, the daily rainfall amounts (light blue bars) are reported.

In Figure 8b, the variation of d-excess measured in shallow and deep wells is reported. The deuterium excess ( $\text{d-excess} = \delta\text{D} - 8 \times \delta^{18}\text{O}$ , [90]) is a proxy to infer information about the physical conditions at the time of water vapor formation which influences the isotopic signature of the precipitation [91–93]. In the study area, there are no significant differences between shallow and deep wells in all sampling campaigns, indicating a common recharge for the two aquifers. Nevertheless, a seasonal variation of the d-excess can be observed during the recharge and the depletion phases. In particular, in October 2014 (Rs) the lower d-excess values may indicate a recharge likely from less fractionated rainwater from air masses formed in conditions of high relative humidity (RH) typical of the Mediterranean basin during summer months when evaporation is at its maximum. Moreover, during the recharge period, the d-excess is higher, indicating a recharge occurring from rains originating from the western Mediterranean basin, as can be also observed from the vicinity of the shallow and deep wells' isotopic signatures regarding the Mt. Vesuvius MWL (Figure 8a).

The recharge altitude of shallow and deep groundwater can be roughly estimated applying the empirical equation for the  $\delta^{18}\text{O}$  altitude gradient ( $\delta^{18}\text{O} = -5.74 - 0.0026z + 1.144 \times 10^{-6}z^2$ ) found by Madonia et al. [82] for Mount Vesuvius, which is close to the study area (Figure 1a). The mean recharge altitude of groundwater in the *Cumae* archeological site has been estimated to be about 200 m a.s.l. considering an average annual  $\delta^{18}\text{O}$  value ( $n = 93$ ) of  $-6.22 \pm 0.8\text{‰}$ , which confirms the local recharge of the aquifer inferred by the seasonal isotopic variations observed.

In order to study the impact of agriculture, which is the prevalent anthropic activity in the study area (see Figure 1d), the distribution of nitrate was measured in deep and shallow wells and is reported in the box plot of Figure 5e. Generally, groundwater in the study area has a nitrate concentration lower than 20 mg/L, regardless of whether sampled in deep or shallow wells. The exceptions are represented by P1, P3, and P7 among the deep wells and P11 among the shallow wells, which have a concentration of nitrates above 50 mg/L (see Table S1 and Figure 9a). In the study area,  $\delta^{15}\text{N-NO}_3$  composition ranged from 0.6‰ to 23.4‰, while  $\delta^{18}\text{O-NO}_3$  composition ranged from  $-2.6\text{‰}$  to 26.8‰. In Figure 9a, the  $\delta^{18}\text{O-NO}_3$  vs.  $\delta^{15}\text{N-NO}_3$  diagram (after [25]) indicates that the major sources of nitrate are synthetic fertilizers and only to a minor extent manure and septic waste in both shallow and deep wells. In the diagram, a denitrification trend can be clearly seen for the depressed area of the plain,

where groundwater flow slows down and the substrate is rich in organic matter typical for retro-dunal environments (Figure 3). The denitrification process affecting groundwater sampled in wells P5, P8 and P10 strongly attenuates nitrate concentration enriching the heavy isotope. This is further confirmed if the regression of  $\delta^{15}\text{N-NO}_3$  vs.  $\ln[\text{NO}_3]$  is a straight line and the slope quantifies the enrichment factor ( $\epsilon$ ) [25,94]. In particular, in Figure 9b the  $\delta^{15}\text{N-NO}_3$  vs.  $\ln[\text{NO}_3]$  regression analysis of shallow and deep wells indicates that during both the Rc and the Rs periods groundwater flows toward the denitrification area [95]. The denitrification process is more evident during the Rs phase when the enrichment factor  $\epsilon$  ranges from  $-6.5\text{‰}$  to  $-4.6\text{‰}$  with a regression coefficient  $R^2 > 0.8$ .

In Figure 9c, the  $\delta^{11}\text{B}$  compositions measured in groundwater sampled in shallow and deep wells are plotted vs. the B/Cl molar ratios (after [10]) during the Rc and the Rs periods. The plot shows that groundwater in the study area is mostly mixed with hydrothermal waters influenced by the rise of magmatic fluids. The P11 well, localized upstream of the study area, is characterized by more enriched  $\delta^{11}\text{B}$  values, which could indicate a diffuse fertilizer leaching to groundwater throughout the hydrological year due to agricultural drainage. It is worth noting the behavior of the P1 and P3 wells which during the wet period are characterized by more enriched  $\delta^{11}\text{B}$  values with respect to the dry period when pumping is enhanced (P1: from  $4.00\text{‰}$  to  $-0.19\text{‰}$  and P3: from  $7.15\text{‰}$  to  $2.66\text{‰}$ , respectively) showing a mixing with the hydrothermal component more than seawater ( $\delta^{11}\text{B}_{\text{SW}} = 39\text{‰}$ ). Hence, the salinization of the deep aquifer observed in the dry season (EC from  $1.7\text{ mS/cm}$  to  $2.4\text{ mS/cm}$  in P1 and from  $1.0\text{ mS/cm}$  to  $3.9\text{ mS/cm}$  in P3, see Table S1) is likely due to a mixing with deep waters which have been in contact with hydrothermal fluids. The latter hypothesis is further sustained by the plot in Figure 9d where  $\delta^{11}\text{B}$  is plotted vs.  $r[\text{Cl/Mg}]$ , evidencing a mixing between two end-members: groundwater sampled in P11 and in P8/P10. P11 is located upstream of the study site where the aquifer is unconfined and not yet stratified (Figure 2a,b). In the plot, shallow and deep wells are plotted between the end-members and are characterized by almost constant values of the considered parameters in the dry and the wet seasons, with the exception of P1 and P3. In addition, the plot reports the  $[\text{F}^-]$  concentration measured in each well to support the hypothesis of the hydrothermal origin of the waters. In general, an increase in the  $[\text{F}^-]$  values is observed from P11 and P8/P10 and P1 and P3 are characterized by a shift toward the more depleted  $\delta^{11}\text{B}$  values, and increased  $r[\text{Cl/Mg}]$  and  $[\text{F}^-]$  from the Rc to the Rs phase.



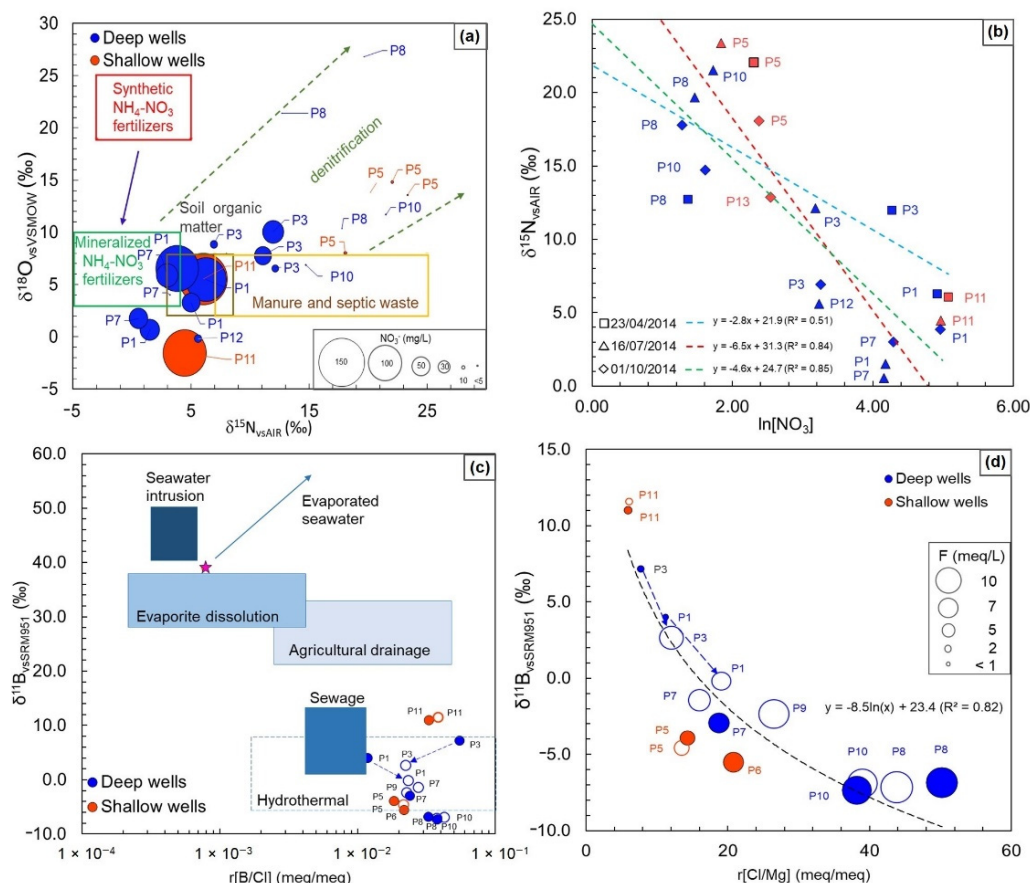


**Figure 9.** (a)  $\delta^{18}\text{O}$  vs.  $\delta^{15}\text{N}$  of dissolved nitrate in shallow (red bubbles) and deep (blue bubbles) wells. The area of the bubbles is proportional to  $[\text{NO}_3^-]$ . The boxes represent the nitrate sources isotopic fingerprint (after [25]). (b) Cross-plot of the  $\delta^{15}\text{N}$  composition of dissolved  $\text{NO}_3$  vs. the natural log of N- $\text{NO}_3$  concentrations (in mg/L) in shallow (red) and deep (blue) wells in the recharge (23 April 2014) and the depletion (16 July 2014, 01 October 2014) periods. (c)  $\delta^{11}\text{B}$  vs.  $r[\text{B/Cl}]$  (after [10]) in shallow (red) and deep (blue) wells plot in the recharge (April 2014, closed circles) and the depletion (July 2014, open circles) periods. The boxes represent the typical sources values; the pink star is seawater (SW). (d)  $\delta^{11}\text{B}$  vs.  $r[\text{Cl/Mg}]$  in shallow (red) and deep (blue) wells in the recharge (April 2014, closed bubbles) and the depletion (July 2014, open bubbles) periods. The area of the bubbles is proportional to  $[\text{F}^-]$ .

## 5. Discussion

A conceptual model of natural and anthropogenic groundwater contamination processes observed in the archaeological site of Cumae is summarized in Figure 10. In Figure 10, the hydrogeological–hydrochemical isotope features in relation to local land use, coastal volcanic–sedimentary environment, and hydrogeological characteristics of the aquifer system are represented.

The eastern sector is characterized by a single unconfined aquifer and a regional W-E oriented groundwater flow orthogonal to the shoreline (Figure 10a), within fractured volcanic relief. Toward the coastal plain, at the site scale, a porous two-layered aquifer system has been found (Figure 2a,b and Figure 10a), formed by a shallow phreatic aquifer and a semiconfined deep aquifer, locally separated by a lithic tuffaceous aquitard (YT). In the coastal zone, the groundwater circulation becomes unitary again within the shallow unconfined aquifer, with the YT aquitard missing.

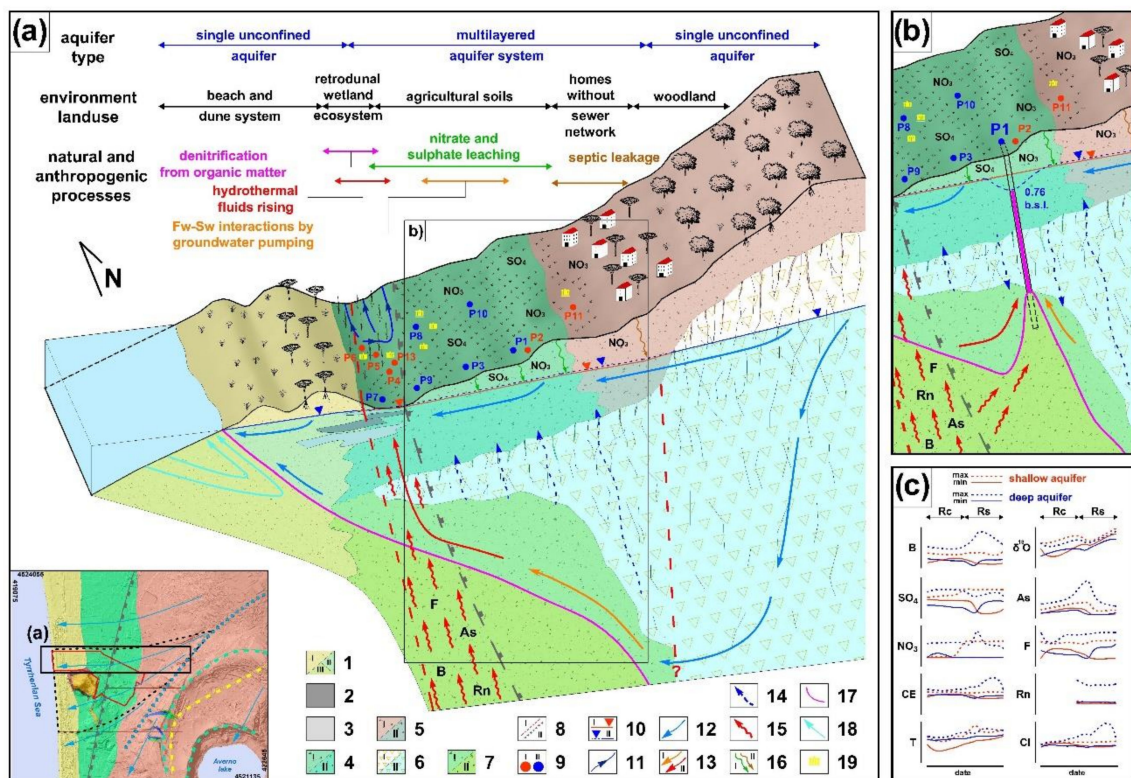


**Figure 10.** Hydrogeological–hydrogeochemical isotope conceptual model of study area, in natural conditions (a) and during pumping (b). (c) Trends of parameters showed in Figure 5, reporting maximum and minimum values of shallow (in red) and deep (in blue) wells with reference to the Rc and Rs periods. The blue and red arrows depict the groundwater flow paths within the aquifer system. The blue arrows indicate shallow groundwater and the red arrows indicate deeper and mineralized groundwater, which interact with the hydrothermal fluids upwelling along deep fractured zone of the CI caldera boundary. Legend: (1) unsaturated (i), freshwater saturated (ii) and saltwater saturated (iii) dune complex; (2) clays and peaty deposits; (3) silts; (4) unsaturated (i) and freshwater saturated (ii) PAP complex; (5) unsaturated (i) and freshwater saturated (ii) P complex; (6) unsaturated (i) and freshwater saturated (ii) YT aquitard; (7) freshwater saturated (i) and saltwater saturated (ii) DP complex; (8) buried normal fault (i) and CI caldera boundary (ii); (9) shallow (i) and deep (ii) wells; (10) piezometric level of phreatic shallow aquifer (i) and deep semiconfined aquifer (ii); (11) groundwater draining channel; (12) groundwater flow direction; (13) mineralized (i) and highly mineralized (ii) groundwater flow direction; (14) vertical groundwater flow direction; (15) high mineralized fluids rising; (16) sulfates and nitrates infiltration from agricultural lands (i) and urban areas (ii); (17) Fw-Sw interface; (18) saline groundwater flow; (19) archaeological site of Monumental Roman Necropolis.

Piezometric monitoring indicated that during the Rc period groundwater flow in the semiconfined aquifer is directed upwards, recharging the shallow aquifer. This hydrogeological evidence has been confirmed by hydrochemical and isotopic data which highlighted a common origin for the shallow and deep groundwater. In particular, groundwater flowing in the two-layered aquifer is recharged locally (mean recharging altitude: 200 m.a.s.l.) and has a short residence time as indicated by water stable isotopes.

Nevertheless, the semiconfined deeper aquifer, if compared with the shallow aquifer (Figure 10c), is characterized throughout the hydrological year by more mineralized groundwater with significantly higher EC and temperature as well as elevated concentrations of chloride, fluoride, boron, arsenic, and  $^{222}\text{Rn}$  (Figure 10c), especially in the wells in the central sector of the coastal plain (see P7, P8, P9 and P10 in Figure 10a).

At the local scale, the mineralization observed in shallow and deep wells is strongly influenced by natural processes due to the rise along buried normal faults and deep fractured zones of the western edge of CI caldera boundaries of mineralized magmatic fluids (Figure 10a). Moreover, in some shallow and deep wells (P5, P8, P10 in Figure 10a) located in the drained retro-dunal area of the coastal plain, where groundwater flow slows down and the aquifer lithology is rich in organic matter, a denitrification trend has been highlighted by means of  $\delta^{18}\text{O}\text{-NO}_3$  and  $\delta^{15}\text{N}\text{-NO}_3$ .

The anthropic groundwater contamination is mostly due to non-point agricultural sources and leaking from local septic tanks. High concentrations of nitrate and sulphate have been found in the upstream and recharge areas (well P11) and in a few deep wells (wells P1, P3 and P7). The major source of nitrate is synthetic fertilizers and to lesser extent manure and septic waste in both shallow and deep wells. Finally, in the drawdown period (Figure 10b), when pumping of groundwater used for irrigation lowers hydraulic head in the deep aquifer in correspondence to P1 and P3 agricultural wells, local vertical groundwater flow is reversed and the shallow groundwater leaks. The hydrochemical and isotopic data reveal that groundwater in the two deep wells is highly mineralized, reaching the highest values of EC, chloride, fluoride, boron, arsenic, and  $^{222}\text{Rn}$  (Figure 10c), indicating a mixing with more mineralized groundwater of hydrothermal origin and to a minor extent to the mixing with seawater, clearly evidenced by the isotopic ratios of boron.

## 6. Concluding Remarks

The main purpose of the present study was to investigate, by means of a multidisciplinary approach, a whole hydrologic year to comprehensively assess for the first time the main natural and anthropogenic processes influencing, at the site scale, groundwater quality in the *Cumae* archaeological site with a catchment approach.

Hydrogeological monitoring confirms the presence of a complex coastal volcanic-sedimentary system, whereas all the hydrochemical and isotopic observations show that the groundwater quality is affected mainly by: (i) aquifer lithology and localized rise of mineralized magmatic fluids along buried normal faults of the CI caldera boundary, (ii) interaction and mixing between shallow groundwater, deeper mineralized groundwater and saltwater intrusion during groundwater pumping, and (iii) contamination from non-point agricultural sources.

$\delta\text{D}$  and  $\delta^{18}\text{O}$  data show a fast recharge from seasonal precipitations originating from evaporated and re-evaporated air masses.

Chemical data evidence nitrate pollution ( $>50\text{ mg L}^{-1}$ ) occurring mainly in the deep semiconfined aquifer. Isotopic ratios of N and O in dissolved nitrates evidence the contribution of different possible sources: natural, mineral fertilizers and, to a minor extent, manure and possible leaks from septic tanks or sewage systems.

Moreover, in the low lying and drained retro-dunal area of the coastal plain, denitrification processes are highlighted both in the shallow and the deep aquifers.

In conclusion, this study can be considered a valuable contribution to the comprehension of the natural and anthropogenic dynamics of groundwater contamination in the complex coastal volcanic-sedimentary system which hosts one of the most visited archaeological sites in southern Italy. The results obtained are a useful tool to assist and help the local archaeological authority in addressing the problems deriving from groundwater flooding and in decision-making aimed to safeguard and manage the archaeological heritage of the *Cumae* site.

**Supplementary Materials:** The following are available online at <http://www.mdpi.com/2073-4441/12/12/3463/s1>, Table S1: Hydrogeological, hydrochemical and isotopic monitoring data of groundwater in the *Cumae* archaeological site.

**Author Contributions:** Conceptualization, V.A., L.S. and S.C.; methodology, V.A., L.S. and S.C.; software, V.A., L.S. and S.C. and validation, V.A., L.S., and S.C.; formal analysis, V.A., L.S., and S.C.; investigation, V.A., L.S., L.F., M.A., P.D.V., and B.D.R.; resources, financial support from Univ. of Naples “Federico II” and Univ. of Campania “Luigi Vanvitelli”; data curation, L.S., S.C. and V.A.; writing—original draft preparation, V.A., L.S., S.C. and writing—review and editing, V.A., L.S., S.C., P.D.V., M.T., F.M., A.D., B.D.R., L.F. and M.A.; visualization, V.A. and



L.S.; supervision, V.A. and L.S.; project administration, V.A., L.S. and S.C. All authors have read and agreed to the published version of the manuscript.

**Funding:** This research received no external funding

**Acknowledgments:** The authors wish to thank P. Caputo and C. Giordano of the Soprintendenza per i Beni Archeologici di Napoli (Cuma Office), for their collaboration for the development of the field groundwater monitoring at the archaeological site of *Cumae*. The authors wish to thank Valentina Di Maio and Antonella Gaeta for their collaboration during groundwater sampling and field monitoring. Finally, the authors greatly acknowledge the anonymous reviewer for his precious suggestions and comments which improved the quality of the final version of the manuscript.

**Conflicts of Interest:** The authors declare no conflict of interest.

## References

1. Zepeda Quintana, D.S.; Loeza Rentería, C.M.; Munguía Vega, N.E.; Peralta, J.E.; Velazquez Contreras, L.E. Sustainability strategies for coastal aquifers: A case study of the Hermosillo Coast aquifer. *J. Clean. Prod.* **2018**, *195*, 1170–1182. [\[CrossRef\]](#)
2. Unsal, B.; Yagbasan, O.; Yazicigil, H. Assessing the impacts of climate change on sustainable management of coastal aquifers. *Environ. Earth Sci.* **2014**, *72*, 2183–2193. [\[CrossRef\]](#)
3. Chatton, E.; Aquilina, L.; Pételet-Giraud, E.; Cary, L.; Bertrand, G.; Labasque, T.; Hirata, R.; Martins, V.; Montenegro, S.; Vergnaud, V.; et al. Glacial recharge, salinisation and anthropogenic contamination in the coastal aquifers of Recife (Brazil). *Sci. Total Environ.* **2016**, *569–570*, 1114–1125. [\[CrossRef\]](#) [\[PubMed\]](#)
4. Ferguson, G.; Gleeson, T. Vulnerability of coastal aquifers to groundwater use and climate change. *Nat. Clim. Chang.* **2012**, *2*, 342–345. [\[CrossRef\]](#)
5. Renau-Pruñonosa, A.; Morell, I.; Pulido-Velazquez, D. A Methodology to Analyse and Assess Pumping Management Strategies in Coastal Aquifers to Avoid Degradation Due to Seawater Intrusion Problems. *Water Resour. Manag.* **2016**, *30*, 4823–4837. [\[CrossRef\]](#)
6. IPCC. 2007: *Climate Change 2007: The Physical Science Basis. Contribution of Working Group I to the Fourth Assessment Report of the Intergovernmental Panel on Climate Change*; Solomon, S., Qin, D., Manning, M., Chen, Z., Marquis, M., Averyt, K.B., Tignor, M., Miller, H.L., Eds.; Cambridge University Press: Cambridge, UK; New York, NY, USA, 2007; ISBN 978-0-521-88009-1.
7. Russak, A.; Sivan, O. Hydrogeochemical Tool to Identify Salinization or Freshening of Coastal Aquifers Determined from Combined Field Work, Experiments, and Modeling. *Environ. Sci. Technol.* **2010**, *44*, 4096–4102. [\[CrossRef\]](#)
8. Werner, A.D.; Bakker, M.; Post, V.E.A.; Vandenbohede, A.; Lu, C.; Ataie-Ashtiani, B.; Simmons, C.T.; Barry, D.A. Seawater intrusion processes, investigation and management: Recent advances and future challenges. *Adv. Water Resour.* **2013**, *51*, 3–26. [\[CrossRef\]](#)
9. Colombani, N.; Osti, A.; Volta, G.; Mastrocicco, M. Impact of Climate Change on Salinization of Coastal Water Resources. *Water Resour. Manag.* **2016**, *30*, 2483–2496. [\[CrossRef\]](#)
10. Vengosh, A. Salinization and Saline Environments. In *Treatise on Geochemistry*; Holland, H.D., Turekian, K.K., Eds.; Pergamon: Oxford, UK, 2003; pp. 1–35, ISBN 978-0-08-043751-4.
11. Custodio, E. Coastal aquifers of Europe: An overview. *Hydrogeol. J.* **2010**, *18*, 269–280. [\[CrossRef\]](#)
12. Kim, Y.; Lee, K.-S.; Koh, D.-C.; Lee, D.-H.; Lee, S.-G.; Park, W.-B.; Koh, G.-W.; Woo, N.-C. Hydrogeochemical and isotopic evidence of groundwater salinization in a coastal aquifer: A case study in Jeju volcanic island, Korea. *J. Hydrol.* **2003**, *270*, 282–294. [\[CrossRef\]](#)
13. Carreira, P.M.; Marques, J.M.; Nunes, D. Source of groundwater salinity in coastline aquifers based on environmental isotopes (Portugal): Natural vs. human interference. A review and reinterpretation. *Appl. Geochem.* **2014**, *41*, 163–175. [\[CrossRef\]](#)
14. Pastén-Zapata, E.; Ledesma-Ruiz, R.; Harter, T.; Ramírez, A.I.; Mahlknecht, J. Assessment of sources and fate of nitrate in shallow groundwater of an agricultural area by using a multi-tracer approach. *Sci. Total Environ.* **2014**, *470–471*, 855–864. [\[CrossRef\]](#)
15. Lin, J.K. Nitrosamines as potential environmental carcinogens in man. *Clin. Biochem.* **1990**, *23*, 67–71. [\[CrossRef\]](#)
16. Tricker, A.R.; Preussmann, R. Carcinogenic N-nitrosamines in the diet: Occurrence, formation, mechanisms and carcinogenic potential. *Mutat. Res. Genet. Toxicol.* **1991**, *259*, 277–289. [\[CrossRef\]](#)

17. Aravena, R.; Evans, M.L.; Cherry, J.A. Stable Isotopes of Oxygen and Nitrogen in Source Identification of Nitrate from Septic Systems. *Groundwater* **1993**, *31*, 180–186. [[CrossRef](#)]
18. Zhang, Q.; Wang, H.; Wang, L. Tracing nitrate pollution sources and transformations in the over-exploited groundwater region of north China using stable isotopes. *J. Contam. Hydrol.* **2018**, *218*, 1–9. [[CrossRef](#)]
19. Kitsiou, D.; Karydis, M. Coastal marine eutrophication assessment: A review on data analysis. *Environ. Int.* **2011**, *37*, 778–801. [[CrossRef](#)]
20. Zhou, Y.; Wang, L.; Zhou, Y.; Mao, X. Eutrophication control strategies for highly anthropogenic influenced coastal waters. *Sci. Total Environ.* **2020**, *705*, 135760. [[CrossRef](#)]
21. Braun, E.; UNEP; The Woods Hole Research Centre. *Reactive Nitrogen in the Environment: Too Much or Too Little of a Good Thing*; UNEP/Earthprint: Paris, France, 2007; ISBN 978-92-807-2783-8.
22. Nord, A.G.; Tronner, K.; Mattsson, E.; Borg, G.C.; Ullén, I. Environmental Threats to Buried Archaeological Remains. *Ambio* **2005**, *34*, 256–262. [[CrossRef](#)]
23. De Beer, H.; Matthiesen, H. Groundwater monitoring and modelling from an archaeological perspective: Possibilities and challenges. In *Geology for Society*; Slagstad, T., Ed.; Geological Survey of Norway Special Publication; Geological Survey of Norway: Trondheim, Norway, 2008; pp. 67–81.
24. Kreyns, P.; Geng, X.; Michael, H.A. The influence of connected heterogeneity on groundwater flow and salinity distributions in coastal volcanic aquifers. *J. Hydrol.* **2020**, *586*, 124863. [[CrossRef](#)]
25. Kendall, C. Tracing Nitrogen Sources and Cycling in Catchments. In *Isotope Tracers in Catchment Hydrology*; Kendall, C., McDonnell, J.J., Eds.; Elsevier: Amsterdam, The Netherlands, 1998; pp. 519–576, ISBN 978-0-444-81546-0.
26. Custodio, E. Effects of human activities on salt–fresh water relationships in coastal aquifers. In *Groundwater Problems in Coastal Areas*; Custodio, E., Bruggeman, G.A., Eds.; Studies and Reports in Hydrology; UNESCO: Paris, France, 1987.
27. Petelet-Giraud, E.; Négrel, P.; Aunay, B.; Ladouche, B.; Bailly-Comte, V.; Guerrot, C.; Flehoc, C.; Pezard, P.; Lofi, J.; Dörfli, N. Coastal groundwater salinization: Focus on the vertical variability in a multi-layered aquifer through a multi-isotope fingerprinting (Roussillon Basin, France). *Sci. Total Environ.* **2016**, *566–567*, 398–415. [[CrossRef](#)] [[PubMed](#)]
28. Zhao, Q.; Su, X.; Kang, B.; Zhang, Y.; Wu, X.; Liu, M. A hydrogeochemistry and multi-isotope (Sr, O, H, and C) study of groundwater salinity origin and hydrogeochemical processes in the shallow confined aquifer of northern Yangtze River downstream coastal plain, China. *Appl. Geochem.* **2017**, *86*, 49–58. [[CrossRef](#)]
29. Abu Al Naeem, M.F.; Yusoff, I.; Ng, T.F.; Maity, J.P.; Alias, Y.; May, R.; Alborsh, H. A study on the impact of anthropogenic and geogenic factors on groundwater salinization and seawater intrusion in Gaza coastal aquifer, Palestine: An integrated multi-techniques approach. *J. Afr. Earth Sci.* **2019**, *156*, 75–93. [[CrossRef](#)]
30. Vengosh, A.; Spivack, A.J.; Artzi, Y.; Ayalon, A. Geochemical and boron, strontium, and oxygen isotopic constraints on the origin of the salinity in groundwater from the Mediterranean Coast of Israel. *Water Resour. Res.* **1999**, *35*, 1877–1894. [[CrossRef](#)]
31. Stellato, L. Isotopic Methodologies: A Valuable Tool to Study Stream Water–Groundwater Interactions. In *Horizons in Earth Science Research*; Veress, B., Szigethy, J., Eds.; Nova Science Publishers: New York, NY, USA, 2010; Volume 1, pp. 239–260, ISBN 978-1-60741-221-2.
32. De Giorgio, G.; Chieco, M.; Zuffianò, L.E.; Limoni, P.P.; Sottani, A.; Pedron, R.; Vettorello, L.; Stellato, L.; Di Rienzo, B.; Polemio, M. The Compatibility of Geothermal Power Plants with Groundwater Dependent Ecosystems: The Case of the Cesine Wetland (Southern Italy). *Sustainability* **2018**, *10*, 303. [[CrossRef](#)]
33. Martinelli, G.; Dadomo, A.; De Luca, D.A.; Mazzola, M.; Lasagna, M.; Pennisi, M.; Pilla, G.; Sacchi, E.; Saccon, P. Nitrate sources, accumulation and reduction in groundwater from Northern Italy: Insights provided by a nitrate and boron isotopic database. *Appl. Geochem.* **2018**, *91*, 23–35. [[CrossRef](#)]
34. Ducci, D.; Del Gaudio, E.; Sellerino, M.; Stellato, L.; Corniello, A. Hydrochemical and isotopic analyses to identify groundwater nitrate contamination. The alluvial-pyroclastic aquifer of the Campanian plain (southern Italy). *Geog. Ambient. Min.* **2019**, *156*, 4–12.
35. Wood, W.W.; Sanford, W.E. Chemical and isotopic methods for quantifying ground-water recharge in a regional, semiarid environment. *Ground Water* **1995**, *33*, 458–469. [[CrossRef](#)]
36. Gonfiantini, R.; Fröhlich, K.; Araguás-Araguás, L.; Rozanski, K. Isotopes in Groundwater Hydrology. In *Isotope Tracers in Catchment Hydrology*; Kendall, C., McDonnell, J.J., Eds.; Elsevier: Amsterdam, The Netherlands, 1998; pp. 203–246, ISBN 978-0-444-81546-0.

37. Thyne, G.D.; Gillespie, J.M.; Ostdick, J.R. Evidence for interbasin flow through bedrock in the southeastern Sierra Nevada. *GSA Bull.* **1999**, *111*, 1600–1616. [\[CrossRef\]](#)
38. Coplen, T.B.; Herczeg, A.L.; Barnes, C. Isotope Engineering—Using Stable Isotopes of the Water Molecule to Solve Practical Problems. In *Environmental Tracers in Subsurface Hydrology*; Cook, P.G., Herczeg, A.L., Eds.; Springer: Boston, MA, USA, 2000; pp. 79–110, ISBN 978-1-4615-4557-6.
39. Herczeg, A.L.; Edmunds, W.M. Inorganic Ions as Tracers. In *Environmental Tracers in Subsurface Hydrology*; Cook, P.G., Herczeg, A.L., Eds.; Springer: Boston, MA, USA, 2000; pp. 31–77, ISBN 978-1-4615-4557-6.
40. Genereux, D.P.; Wood, S.J.; Pringle, C.M. Chemical tracing of interbasin groundwater transfer in the lowland rainforest of Costa Rica. *J. Hydrol.* **2002**, *258*, 163–178. [\[CrossRef\]](#)
41. Richter, B.C.; Kreitler, C.W. *Geochemical Techniques for Identifying Sources of Ground-Water Salinization*; Smoley, C.K., Ed.; CRC Press: Austin, TX, USA, 1993; ISBN 978-1-56670-000-9.
42. Stellato, L.; Petrella, E.; Terrasi, F.; Belloni, P.; Belli, M.; Sansone, U.; Celico, F. Some limitations in using  $^{222}\text{Rn}$  to assess river–groundwater interactions: The case of Castel di Sangro alluvial plain (central Italy). *Hydrogeol. J.* **2008**, *16*, 701–712. [\[CrossRef\]](#)
43. Stellato, L.; Terrasi, F.; Marzaioli, F.; Belli, M.; Sansone, U.; Celico, F. Is  $^{222}\text{Rn}$  a suitable tracer of stream–groundwater interactions? A case study in central Italy. *Appl. Geochem.* **2013**, *32*, 108–117. [\[CrossRef\]](#)
44. Wu, S.-F.; You, C.-F.; Lin, Y.-P.; Valsami-Jones, E.; Baltatzis, E. New boron isotopic evidence for sedimentary and magmatic fluid influence in the shallow hydrothermal vent system of Milos Island (Aegean Sea, Greece). *J. Volcanol. Geotherm. Res.* **2016**, *310*, 58–71. [\[CrossRef\]](#)
45. Liu, M.; Guo, Q.; Wu, G.; Guo, W.; She, W.; Yan, W. Boron geochemistry of the geothermal waters from two typical hydrothermal systems in Southern Tibet (China): Daggyai and Quzhuomu. *Geothermics* **2019**, *82*, 190–202. [\[CrossRef\]](#)
46. Vengosh, A.; Heumann, K.G.; Juraske, S.; Kashner, R. Boron Isotope Application for Tracing Sources of Contamination in Groundwater. *Environ. Sci. Technol.* **1994**, *28*, 1968–1974. [\[CrossRef\]](#)
47. Widory, D.; Kloppmann, W.; Chery, L.; Bonnin, J.; Rochdi, H.; Guinamant, J.-L. Nitrate in groundwater: An isotopic multi-tracer approach. *J. Contam. Hydrol.* **2004**, *72*, 165–188. [\[CrossRef\]](#)
48. Xue, D.; Botte, J.; De Baets, B.; Accoe, F.; Nestler, A.; Taylor, P.; Van Cleemput, O.; Berglund, M.; Boeckx, P. Present limitations and future prospects of stable isotope methods for nitrate source identification in surface- and groundwater. *Water Res.* **2009**, *43*, 1159–1170. [\[CrossRef\]](#)
49. Allocca, V.; Celico, P. Scenari idrodinamici nella piana ad Oriente di Napoli (Italia) nell’ultimo secolo: Cause e problematiche idrogeologiche connesse. *G. Di Geol. Appl.* **2008**, *9*, 175. [\[CrossRef\]](#)
50. Allocca, V.; Coda, S.; De Vita, P.; Iorio, A.; Viola, R. Rising groundwater levels and impacts in urban and semirural area around Naples (southern Italy). *Rend. Soc. Geol. It.* **2016**, *41*, 14–17. [\[CrossRef\]](#)
51. Coda, S.; Tessitore, S.; Di Martire, D.; De Vita, P.; Allocca, V. Environmental effects of the groundwater rebound in the eastern plain of Naples (Italy). *Rend. Soc. Geol. It.* **2019**, *48*, 35–40. [\[CrossRef\]](#)
52. Abdallah, I.M.; Abd El-Tawab, N.A. Effects of the groundwater on deterioration of the catacombs of Kom El-Shoqafa, Alexandria, Egypt. *E Conserv.* **2013**, 168–181.
53. Caputo, P.; Morichi, R.; Paone, R. *Cuma e il Suo Parco Archeologico. Un Territorio E le Sue Testimonianze*; Scienze e Lettere; Bardi Ed.: Rome, Italy, 2010; ISBN 978-88-88620-87-9.
54. Capano, M.; Rescigno, C.; Sirleto, R.; Passariello, I.; Marzaioli, F.; D’Onofrio, A.; Terrasi, F. AMS  $^{14}\text{C}$  dating at CIRCE: The Major Temple in Cumae (NA–Italy). *Nucl. Instrum. Methods Phys. Res. Sect. B Beam Interact. Mater. Atoms* **2015**, *361*, 654–658. [\[CrossRef\]](#)
55. Holden, J.; West, L.J.; Howard, A.J.; Maxfield, E.; Panter, I.; Oxley, J. Hydrological controls of in situ preservation of waterlogged archaeological deposits. *Earth Sci. Rev.* **2006**, *78*, 59–83. [\[CrossRef\]](#)
56. Van der Noort, R. Assessment and management of sites in wetland landscapes: Four case studies from the Humber wetlands. In *Preserving Archaeological Remains in Situ*; Corfield, M., Hinton, P., Nixon, T., Pollard, M., Eds.; Museum of London Archaeology Service: London, UK, 1996; pp. 133–143, ISBN 1-56670-000-0.
57. Van De Noort, R.; Chapman, H.P.; Cheetham, J.L. In situ preservation as a dynamic process: The example of Sutton Common, UK. *Antiquity* **2001**, *75*, 94–100. [\[CrossRef\]](#)
58. Sacchi, M.; Molisso, F.; Pacifico, A.; Vigliotti, M.; Sabbarese, C.; Ruberti, D. Late-Holocene to recent evolution of Lake Patria, South Italy: An example of a coastal lagoon within a Mediterranean delta system. *Glob. Planet. Chang.* **2014**, *117*, 9–27. [\[CrossRef\]](#)



59. De Vivo, B.; Rolandi, G.; Gans, P.B.; Calvert, A.; Bohrsen, W.A.; Spera, F.J.; Belkin, H.E. New constraints on the pyroclastic eruptive history of the Campanian volcanic Plain (Italy). *Mineral. Petrol.* **2001**, *73*, 47–65. [\[CrossRef\]](#)
60. Bravi, S.; Fuscaldo, M.; Guarino, P.M.; Schiattarella, M. Evoluzione sedimentaria olocenica dell'area dell'antico porto di Cumae (Campi Flegrei). In *Variazioni Climatico-Ambientali ed Impatto Sull'uomo Nell'area Circum-Mediterranea Durante L'olocene. Territorio Storico ed Ambiente*; EdiPuglia: Bari, Italy, 1996; pp. 23–64.
61. ISPRA. *Note Illustrative Della Carta Geologica d'Italia Alla Scala 1: 50.000, Foglio 446-447 Napoli*; Litografia Artistica Cartografica; APAT, Dipartimento Difesa del Suolo, Servizio Geologico d'Italia: Firenze, Italy, 2015.
62. Celico, P.; Dall'Aglio, M.; Ghiara, M.R.; Stanzione, D.; Brondi, M.; Prosperi, M. Geochemical monitoring of the thermal fluids in the Phlegraean Fields from 1970 to 1990. *Boll. Soc. Geol. Ital.* **1992**, *111*, 409–422.
63. De Vita, P.; Allocca, V.; Celico, F.; Fabbrocino, S.; Mattia, C.; Monacelli, G.; Musilli, I.; Piscopo, V.; Scalise, A.R.; Summa, G.; et al. Hydrogeology of continental southern Italy. *J. Maps* **2018**, *14*, 230–241. [\[CrossRef\]](#)
64. Tufano, R.; Allocca, V.; Coda, S.; Cusano, D.; Fusco, F.; Nicodemo, F.; Pizzolante, A.; De Vita, P. Groundwater vulnerability of principal aquifers of the Campania region (southern Italy). *J. Maps* **2020**, *16*, 565–576. [\[CrossRef\]](#)
65. Allocca, V.; Coda, S.; De Vita, P.; Di Rienzo, B.; Ferrara, L.; Giarra, A.; Mangoni, O.; Stellato, L.; Trifuoggi, M.; Arienzo, M. Hydrogeological and hydrogeochemical study of a volcanic-sedimentary coastal aquifer in the archaeological site of Cumae (Phlegraean Fields, southern Italy). *J. Geochem. Explor.* **2018**, *185*, 105–115. [\[CrossRef\]](#)
66. Allocca, V.; Manna, F.; De Vita, P. Estimating annual groundwater recharge coefficient for karst aquifers of the southern Apennines (Italy). *Hydrol. Earth Syst. Sci.* **2014**, *18*, 803–817. [\[CrossRef\]](#)
67. Coda, S.; Tessitore, S.; Di Martire, D.; Calcaterra, D.; De Vita, P.; Allocca, V. Coupled ground uplift and groundwater rebound in the metropolitan city of Naples (southern Italy). *J. Hydrol.* **2019**, *569*, 470–482. [\[CrossRef\]](#)
68. Coda, S.; Confuorto, P.; De Vita, P.; Di Martire, D.; Allocca, V. Uplift Evidences Related to the Recession of Groundwater Abstraction in a Pyroclastic-Alluvial Aquifer of Southern Italy. *Geosciences* **2019**, *9*, 215. [\[CrossRef\]](#)
69. Lambeck, K.; Anzidei, M.; Antonioli, F.; Benini, A.; Esposito, A. Sea level in Roman time in the Central Mediterranean and implications for recent change. *Earth Planet. Sci. Lett.* **2004**, *224*, 563–575. [\[CrossRef\]](#)
70. Todesco, M.; Costa, A.; Comastri, A.; Colleoni, F.; Spada, G.; Quarenì, F. Vertical ground displacement at Campi Flegrei (Italy) in the fifth century: Rapid subsidence driven by pore pressure drop. *Geophys. Res. Lett.* **2014**, *41*, 1471–1478. [\[CrossRef\]](#)
71. Città Metropolitana di Napoli—Telerilevamento Mediante Lidar. Available online: <http://sit.cittametropolitana.na.it/lidar.html> (accessed on 26 October 2020).
72. U.S. Environmental Protection Agency. *Radon in Water Sampling Program*; EPA/EERF Manual 78-1; U.S. Environmental Protection Agency: Washington, DC, USA, 1978; p. 11.
73. Belloni, P.; Cavaoli, M.; Ingraio, G.; Mancini, C.; Notaro, M.; Santaroni, P.; Torri, G.; Vasselli, R. Optimization and comparison of three different methods for the determination of Rn-222 in water. *Sci. Total Environ.* **1995**, *173–174*, 61–67. [\[CrossRef\]](#)
74. Clark, I.D.; Fritz, P. *Environmental Isotopes in Hydrogeology*; Lewis Publishers: Boca Raton, NY, USA, 1997; ISBN 978-1-56670-249-2.
75. Silva, S.R.; Kendall, C.; Wilkison, D.H.; Ziegler, A.C.; Chang, C.C.Y.; Avanzino, R.J. A new method for collection of nitrate from fresh water and the analysis of nitrogen and oxygen isotope ratios. *J. Hydrol.* **2000**, *228*, 22–36. [\[CrossRef\]](#)
76. Eppich, G.R.; Wimpenny, J.B.; Yin, Q.-Y.; Esser, B.K. *California GAMA Special Study: Stable Isotopic Composition of Boron in Groundwater—Analytical Method Development—Tech. Rep. LLNL-TR-498360*; Lawrence Livermore National Laboratory: Livermore, CA, USA, 2011; p. 29.
77. Ying-Kai, X.; Bu-Yong, L.; Wei-Guo, L.; Yun, X.; George, H.S. Ion Exchange Extraction of Boron from Aqueous Fluids by Amber-lite IRA 743 Resin. *Chin. J. Chem.* **2003**, *21*, 1073–1079. [\[CrossRef\]](#)
78. Baek, K.-W.; Song, S.-H.; Kang, S.-H.; Rhee, Y.-W.; Lee, C.-S.; Lee, B.-J.; Hudson, S.; Hwang, T.-S. Adsorption Kinetics of Boron by Anion Exchange Resin in Packed Column Bed. *J. Ind. Eng. Chem.* **2007**, *13*, 452–456.
79. Langelier, W.F.; Ludwig, H.F. Graphical Methods for Indicating the Mineral Character of Natural Waters. *J. Am. Water Work. Assoc.* **1942**, *34*, 335–352. [\[CrossRef\]](#)

80. Cox, M.E.; Thomas, D.M. Cl/Mg ratio of Hawaiian groundwaters as a regional geothermal indicator. *Geotherm. Resour. Counc. Trans.* **1979**, *3*, 145–148.
81. Aiuppa, A.; Avino, R.; Brusca, L.; Caliro, S.; Chiodini, G.; D'Alessandro, W.; Favara, R.; Federico, C.; Ginevra, W.; Inguaggiato, S.; et al. Mineral control of arsenic content in thermal waters from volcano-hosted hydrothermal systems: Insights from island of Ischia and Phlegrean Fields (Campanian Volcanic Province, Italy). *Chem. Geol.* **2006**, *229*, 313–330. [[CrossRef](#)]
82. Madonia, P.; Federico, C.; Favara, R. Isotopic composition of rain- and groundwater at Mt. Vesuvius: Environmental and volcanological implications. *Environ. Earth Sci.* **2014**, *72*, 2009–2018. [[CrossRef](#)]
83. Rozanski, K.; Araguas-Araguas, L.; Gonfiantini, R. Isotope patterns in modern global precipitation. *Am. Geophys. Union Monogr.* **1993**, *78*, 1–36.
84. Gat, J.R.; Carmi, I. Evolution of the isotopic composition of atmospheric waters in the Mediterranean Sea area. *J. Geophys. Res.* **1970**, *75*, 3039–3048. [[CrossRef](#)]
85. D'Amore, F.; Fancelli, R.; Panichi, C. Stable isotope study of reinjection processes in the Larderello geothermal field. *Geochim. Cosmochim. Acta* **1987**, *51*, 857–867. [[CrossRef](#)]
86. Pauwels, H.; Gaus, I.; le Nindre, Y.M.; Pearce, J.; Czernichowski-Lauriol, I. Chemistry of fluids from a natural analogue for a geological CO<sub>2</sub> storage site (Montmiral, France): Lessons for CO<sub>2</sub>–water–rock interaction assessment and monitoring. *Appl. Geochem.* **2007**, *22*, 2817–2833. [[CrossRef](#)]
87. Cartwright, I.; Weaver, T.; Tweed, S.; Ahearne, D.; Cooper, M.; Czapnik, C.; Tranter, J. O, H, C isotope geochemistry of carbonated mineral springs in central Victoria, Australia: Sources of gas and water–rock interaction during dying basaltic volcanism. *J. Geochem. Explor.* **2000**, *69–70*, 257–261. [[CrossRef](#)]
88. Caliro, S.; Chiodini, G.; Avino, R.; Minopoli, C.; Bocchino, B. Long time-series of chemical and isotopic compositions of Vesuvius fumaroles: Evidence for deep and shallow processes. *Ann. Geophys.* **2011**, *54*. [[CrossRef](#)]
89. Karolytè, R.; Serno, S.; Johnson, G.; Gilfillan, S.M.V. The influence of oxygen isotope exchange between CO<sub>2</sub> and H<sub>2</sub>O in natural CO<sub>2</sub>-rich spring waters: Implications for geothermometry. *Appl. Geochem.* **2017**, *84*, 173–186. [[CrossRef](#)]
90. Dansgaard, W. Stable isotopes in precipitation. *Tellus* **1964**, *16*, 436–468. [[CrossRef](#)]
91. Merlivat, L.; Jouzel, J. Global climatic interpretation of the deuterium–oxygen 18 relationship for precipitation. *J. Geophys. Res. Ocean.* **1979**, *84*, 5029–5033. [[CrossRef](#)]
92. Froehlich, K.; Gibson, J.J.; Aggarwal, P.K. Deuterium excess in precipitation and its climatological significance. In *Study of Environmental Change Using Isotope Techniques*; C&S Paper Series; IAEA: Vienna, Austria, 2002; pp. 54–65.
93. Pfahl, S.; Sodemann, H. What controls deuterium excess in global precipitation? *Clim. Past* **2014**, *10*, 771–781. [[CrossRef](#)]
94. Mariotti, A.; Landreau, A.; Simon, B. 15N isotope biogeochemistry and natural denitrification process in groundwater: Application to the chalk aquifer of northern France. *Geochim. Cosmochim. Acta* **1988**, *52*, 1869–1878. [[CrossRef](#)]
95. Fukada, T.; Hiscock, K.M.; Dennis, P.F.; Grischek, T. A dual isotope approach to identify denitrification in groundwater at a river-bank infiltration site. *Water Res.* **2003**, *37*, 3070–3078. [[CrossRef](#)]

**Publisher's Note:** MDPI stays neutral with regard to jurisdictional claims in published maps and institutional affiliations.



© 2020 by the authors. Licensee MDPI, Basel, Switzerland. This article is an open access article distributed under the terms and conditions of the Creative Commons Attribution (CC BY) license (<http://creativecommons.org/licenses/by/4.0/>).